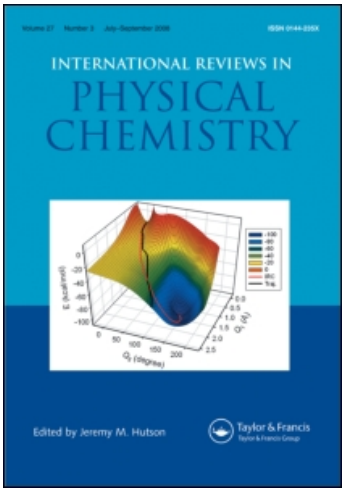

International Reviews in Physical Chemistry
Publication details, including instructions for authors and subscription information:
http://www.informaworld.com/smpp/title~content=t713724383

Observation of anisotropic interactions between metastable atoms and target molecules by two-dimensional collisional ionization electron spectroscopy

Naoki Kishimoto[a]; Koichi Ohno[a]
[a] Department of Chemistry, Graduate School of Science, Tohoku University, Sendai 980-8578, Japan

To cite this Article Kishimoto, Naoki and Ohno, Koichi(2007) 'Observation of anisotropic interactions between metastable atoms and target molecules by two-dimensional collisional ionization electron spectroscopy', International Reviews in Physical Chemistry, 26: 1, 93 — 138
To link to this Article: DOI: 10.1080/01442350601053393
URL: http://dx.doi.org/10.1080/01442350601053393

International Reviews in Physical Chemistry,
Vol. 26, No. 1, January–March 2007, 93–138

Taylor & Francis
Taylor & Francis Group

Observation of anisotropic interactions between metastable atoms and target molecules by two-dimensional collisional ionization electron spectroscopy

NAOKI KISHIMOTO and KOICHI OHNO*

Department of Chemistry, Graduate School of Science, Tohoku University, Aramaki, Aoba-ku, Sendai 980-8578, Japan

(*Received 8 August 2006; in final form 4 October 2006*)

Excited metastable atoms colliding with target molecules can sensitively probe outer properties of molecules by chemi-ionization (Penning ionization) from molecular orbitals in the outer region, since metastable atoms cannot penetrate into the repulsive interaction wall around the molecules. By means of two-dimensional measurements using kinetic energy analysis of electrons combined with a velocity-resolved metastable beam, one can obtain information on the anisotropic interaction between the colliding particles without any control of orientation or alignment of target molecules. We have developed a classical trajectory method to calculate the collision energy dependence of partial ionization cross-sections (CEDPICS) on the anisotropic interaction potential energy surface, which has enabled us to study stereodynamics between metastable atoms and target molecules as well as the spatial distribution of molecular orbitals and electron ejection functions which have a relation with entrance and exit channels of the reaction. Based on the individual CEDPICS, the electronic structure of molecules can also be elucidated.

Contents

*Corresponding author. Email: ohnok@qpcrkk.chem.tohoku.ac.jp

International Reviews in Physical Chemistry
ISSN 0144–235x print/ISSN 1366–591X online
http://www.tandf.co.uk/journals
DOI: 10.1080/01442350601053393

1. Introduction to two-dimensional collisional ionization experiments

Many chemical reactions are induced by collision of reactant species. Their yields, in general, may increase or decrease with collision energy (E_c), which has a strong relation with interaction potentials between the reactant species. For quantitative analyses of chemical reactions, even induced under single collision conditions, one needs to know many aspects of the molecular reaction dynamics [1] such as the interaction potential energy surface, the mechanism of the reaction process, the branching probabilities and the opacity functions, the steric effects in the collisional trajectory, etc. When neutral radical atoms having unpaired electrons collide with molecules, strong attractive interactions with a well depth of several hundred meV or repulsive interactions due to the exchange repulsion can happen. Since interorbital interactions between a colliding

atom and a target molecule are different depending on the energy levels and density distributions of the target molecular orbitals, the interaction potential energy surface between the colliding atom and the target molecule shows a shape with strong anisotropy around the molecule according to the nature of the outer shape of the molecule, which can be probed by projectile atoms [2].

Spectroscopic techniques are useful to measure observables as functions of the energy before and after the chemical reaction. Electron spectroscopic techniques [3–5] have been extensively used to measure ionization energies, which in many cases can be related to electrons ejected from molecular orbitals (MO). Ionization energies observed by ultraviolet photoelectron spectroscopy (UPS) have been compared with theoretical ionization energies [3, 5–7]. Experimental momentum distributions obtained by (e,2e) electron spectroscopy (electron momentum spectroscopy) [8] have been used to compare momentum profiles with those by theoretical MOs [9, 10]. Although ionization of molecules with photons and electrons enables us to study molecular properties by any electron spectroscopic techniques in general, atoms having large excitation energies can probe MOs especially in the chemically important exterior regions, because atoms are only accessible to the exterior parts of target molecules. Details of collisional ionization dynamics have been difficult to understand due to complex processes orginated from anisotropic interactions between the colliding atom and the target molecule. Even in such a case, one may obtain information on the interaction potential from collision-energy-resolved measurements of products, and quantitative agreement between spectroscopic experiments and theory can lead to investigation of the molecular reaction dynamics.

When an excited metastable atom (A*) collides with a target molecule (M), a chemi-ionization process known as Penning ionization [11] can occur to yield an ionic state of M (M_j^+) and the ground state of A together with an ejected electron (e^-);

$$A^* + M \rightarrow A + M_j^+ + e^-. \tag{1}$$

Excitation energies E(A*) of metastable rare gas atoms, such as He*($2^{1,3}$S), Ne*($^3P_{0,2}$), and Ar*($^3P_{0,2}$), are comparable with ultraviolet resonance photon energies of a respective rare gas discharge [12]. The excitation energy difference between a He Iα ultraviolet photon ($E(2^1P \rightarrow 1^1S) = 21.217\,\text{eV}$) and a He*($2^3$S) metastable atom ($E$(He*$2^3$S) = 19.818 eV) is less than 1.4 eV. Extensive studies have been made for Penning ionization with a metastable beam including single-type A* atoms, and the collision energy dependence of total ionization cross-sections (σ_T) by product-ion detection [13] as well as the scattering angular distribution [14] have been measured. Olson showed [15] that the experimental collision energy dependence of the total ionization cross-section for He*($2^{1,3}$S) + Ar was well reproduced by semiempirical calculations based on the theory developed by Nakamura [16] and Miller [17, 18]. In the collision energy region lower than 100 meV, the ionization cross-section decreases with the increase of collision energy, and then starts to increase to 15 Å^2 around a collision energy of 10 eV. The general features of the collision energy dependence of Penning ionization cross-sections are illustrated in figure 1, and they can be classified into three types as follows. The first type (I) is related to the attractive interactions. If the long-range attractive part of the interaction potential $V^*(R)$ as a function of

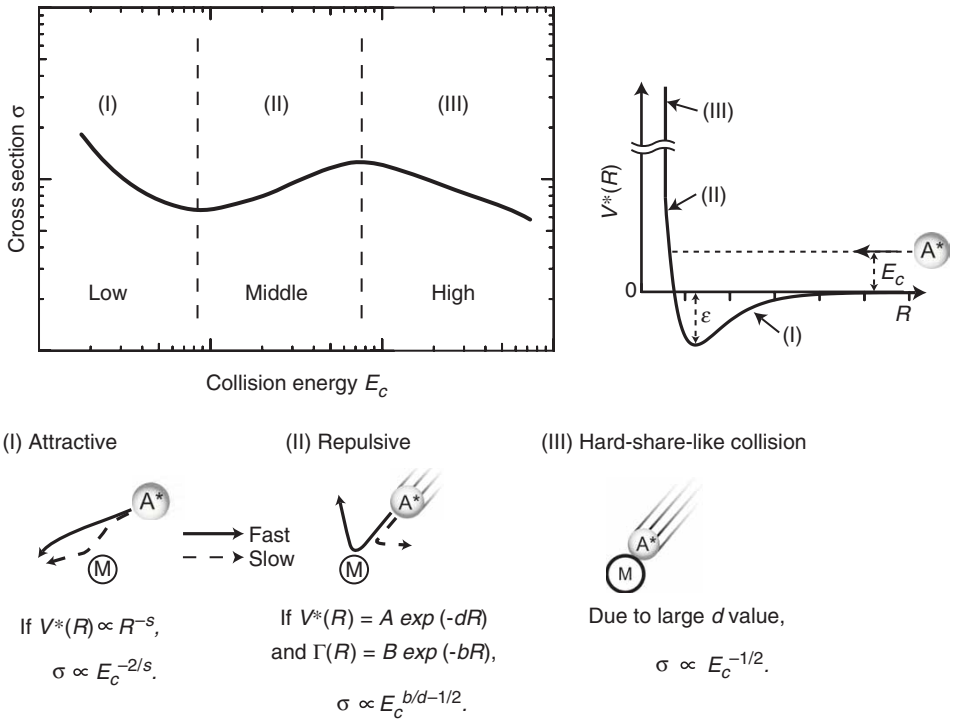

Figure 1. Interaction potential V^* between M and A*, and a curve of collision energy (E_c) dependence of Penning ionization cross-section (σ) in a $\log\sigma - \log E_c$ plot divided into three energetic regions for (I) a negative slope by attractive interaction, (II) a positive slope by repulsive interaction, and (III) a negative slope by hard-sphere-like collision.

distance R, with the potential well ε, plays a dominant role and its function form is the type of

$$V^*(R) \propto R^{-s}, \tag{2}$$

$\sigma_T(E_c)$ can be expressed by

$$\sigma_T(E_c) \propto E_c^{-2/s}. \tag{3}$$

This formula for the Langevin-type cross-section is derived from the impact parameter value at which orbiting occurs. The potential parameter s can be related to interaction forces such as dispersion forces or induced dipole interactions ($s=6$) and ionic interactions ($s=4$). In the second type (II), the repulsive part of the interaction potential governs the collision energy dependence. In the simple theoretical model introduced by Illenberger and Niehaus [19], $\sigma_T(E_c)$ can be expressed as

$$\sigma_T(E_c) \propto \left[\ln\left(\frac{A}{E_c}\right)\right]^2 \left(\frac{E_c}{A}\right)^{(b/d)-(1/2)}, \tag{4}$$

where simple analytical forms of the interaction potential $V^*(R)$ and the ionization width $\Gamma(R)$ are assumed by

$$V^*(R) = A\exp(-dR), \tag{5}$$

and

$$\Gamma(R) = B\exp(-bR). \tag{6}$$

When the minor contribution of the first factor in equation (4) is neglected, the collision energy dependence can be related to d and b via the slope m in a plot of $\log \sigma_T - \log E_c$ by

$$m = \left(\frac{b}{d}\right) - \left(\frac{1}{2}\right). \tag{7}$$

Here, d and b are effective decay parameters of the repulsive potential wall (V^*) and ionization width (Γ), respectively. The third type (III) corresponds to the hard core limit of equation (7); the parameter d becomes considerably large and the slope m of a log $\sigma_T - \log E_c$ plot is nearly $-1/2$. In this case, the effective interaction time deceases with the increase of E_c.

A different type of measurement is electron kinetic energy (E_e) analysis of ejected electrons in Penning ionization, which was known as Penning ionization electron spectroscopy (PIES) [12, 20]. Figure 2 illustrates the relationship between a Penning ionization electron spectrum and the interaction potential energy surfaces of the reactant (entrance channel) and the product (exit channel) for $N_2 + He^*$. The ejected electron energy E_e equals the energy difference of the entrance and the exit potential functions, V^* and V^+, respectively.

$$E_e(R) = V^*(R) - V^+(R). \tag{8}$$

The electron spectroscopic technique enables us to observe different ionic states as well as related MOs of a target molecule. Thus, PIES enabled us to measure partial ionization cross-sections (branching ratios) for respective ionic states from relative band intensities in a Penning ionization electron spectrum.

Since Čermák started PIES in 1966 [20], high-resolution measurements of PIES have been developed for understanding of the ionization processes, and various aspects and suggestions have been reported. Relative enhancement of σ bands in Penning ionization electron spectra for linear molecules was first pointed out by Hotop and Niehaus in 1970 [21]. A remarkable enhancement of 'lone-pair' bands for nitrile compounds was observed, and this finding was ascribed to large electron density localized on the N atom in the relevant orbital [21–23]. Subsequent studies of PIES for π electron systems showed that higher electron densities of the relevant orbitals in the interaction region are most responsible for the observed enhancement of π bands [24, 25]. Careful transmission-corrected PIES measurements of both

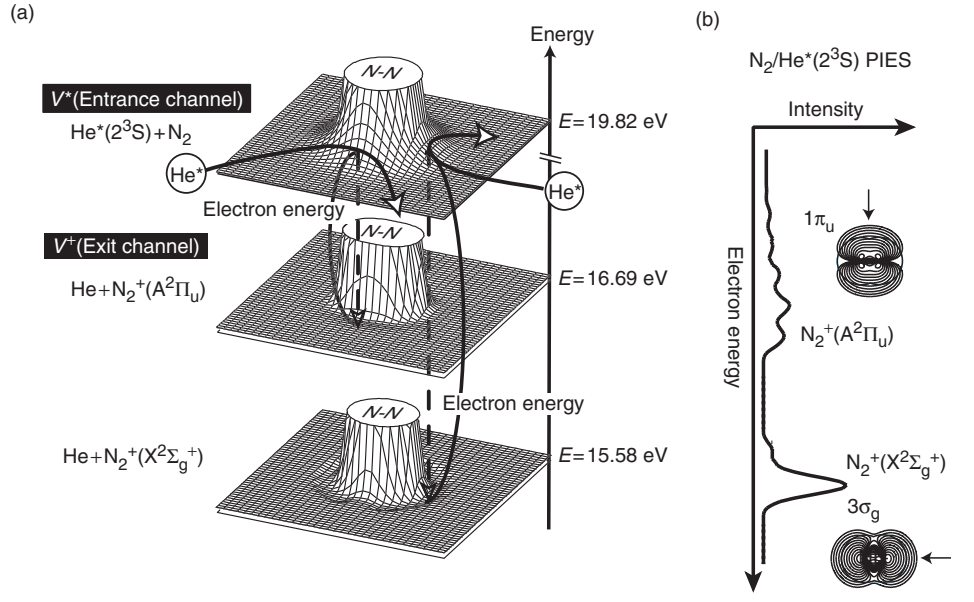

Figure 2. (a) Penning ionization process for $He^* + N_2$. The kinetic energy of the ejected electron equals to the potential energy difference, $V^* - V^+$. The ionization energies of N_2 are taken from He I UPS data [3]. (b) Penning ionization electron spectrum and electron density contour maps of MOs for corresponding ionic states. Arrows indicate the most effective directions for ionization.

organic and inorganic molecules led to the following simple factors governing PIES branching ratios [26, 27]:

1. spatially extended orbitals are more active than spatially limited orbitals;
2. geometrically accessible parts of electron densities of individual molecular orbitals are probed by A*; and
3. relative populations of product ionic states are approximately proportional to the probed electron densities.

The electron density outside the repulsive interaction surface around the molecule (exterior electron density; EED) have been calculated with *ab initio* molecular orbitals and a primitive molecular surface composed of spheres of van der Waals radii [26–29]. Although this molecular surface was very simple, the calculated EED values were comparable with PIES branching ratios of organic molecules such as unsaturated hydrocarbons.

On the other hand, Hotop *et al*. first observed a beam temperature (T) dependence of PIES data for some linear molecules including N_2 and CO in 1979 [30] with two kinds of metastable beam sources at low ($T \sim 400$ K) and high ($T \sim 1000$ K) temperatures. An important feature is the beam temperature dependence of branching ratios; branching ratios for ionization from π orbitals with respect to those from σ orbitals increase with the increase of the beam temperature. This feature was interesting since the different beam temperature dependence of the branching ratios should be connected to strong anisotropic interactions with metastable atoms around the target molecule.

Since the rigid molecular surface may be oversimplified, electronic-state-resolved and collision-energy-resolved measurements of ionization cross-sections were expected to be established.

The total ionization cross-section of a target molecule indicates averaged characteristics of each ionic state, and electronic-state-resolved measurement may enable us to investigate anisotropy of the reaction with partial Penning ionization cross-sections for individual ionic states. In the combined technique of energy selection of both collision energies (E_c) and electron kinetic energies (E_e), either one of these selections of important parameters leads to measurements of

1. collision-energy-resolved Penning ionization electron spectra (CERPIES), and
2. collision energy dependence of partial ionization cross-sections (CEDPICS) for a particular ionic state of M_j^+.

A velocity selected measurement utilizing a time-of-flight (TOF) method with electron spectroscopy was performed for He*(2^3S) + Ar or H in 1979 [31], and velocity-controlled-supersonic metastable He* beams [14] were applied to measurements of CERPIES for Ar [32] and N_2 [33, 34] with the 2^1S state as well as N_2O [35] with the $2^{1,3}$S states. In CERPIES, collision energy dependence can be obtained for the ionic state population, the band width, as well as the peak energy shift. These data can be connected to anisotropic interaction potential energy surfaces for entrance and exit channels, although estimation of the band shape is difficult for some cases. By fixing the electron energy window of the electron energy analyser for a given ionic state, time-dependent Penning electron signals depending on the velocity distribution of a pulsed metastable beam were measured, and CEDPICS of molecules (H_2O, H_2S and O_2) was first reported by our group in 1989 [36]. In order to overcome the low efficiency of signal counts, our efforts were focused on high efficiency measurements of CERPIES as well as CEDPICS. After a few years, we developed a high-intensity He* beam source and observed the anisotropic nature of repulsive interactions around N_2 and CO_2 [37]. With a considerable improvement of data processing units and random access memories (RAM) in the electronic instruments, we have developed multichannel scaler for energy selection of both collisional and electron kinetic energies in 1996 [38], which enabled us to measure both CERPIES and CEDPICS simultaneously by two-dimensional collision-energy/electron-energy-resolved Penning ionization electron spectroscopy (2D-PIES) as shown in figure 3. When the 2D-PIES was combined with a cross-correlation time-of-flight method for a He* metastable beam, highly efficient 2D-PIES measurement was established [39]. Theoretical calculations for partial Penning ionization cross-sections by classical trajectory methods with anisotropic functions of V^* and Γ have also been developed for the analysis of the 2D-PIES data [40, 41].

2. Spatial characteristics of molecular orbitals studied by Penning ionization electron spectroscopy

2.1. *Penning ionization electron spectroscopy and reactivity of molecular orbitals*

The electron kinetic energy distribution in a Penning ionization electron spectrum is similar to that recorded in UPS [3, 5–7]. The observed electron kinetic energies E_e can

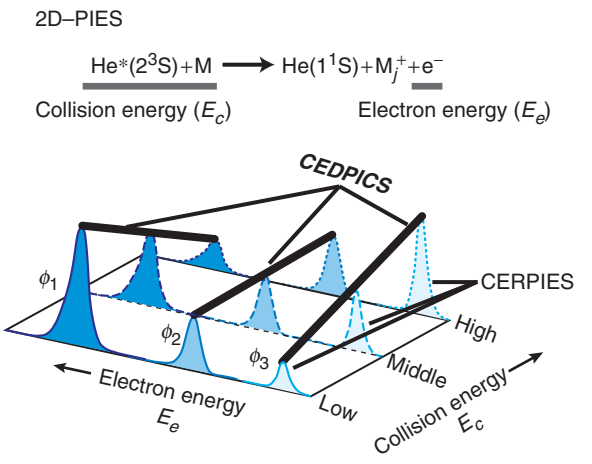

Figure 3. [Colour online] CERPIES (collision-energy-resolved Penning ionization electron spectra) and CEDPICS (collision energy dependence of partial ionization cross-sections) for given values of the collision energy E_c and the electron energy E_e in 2D-PIES, respectively.

be connected to ionization energies I_j by the relation of $E_e = E(A^*) - I_j - \delta_j$, where δ_j is the energy balance due to the relative motion of the rare gas atom and the target molecule [12, 13]. This quantity δ_j, the peak energy shift with respect to the ionization energy, is usually much less than 1 eV. Thus, observed bands in Penning ionization electron spectra can be assigned to individual ionic states corresponding to ionization from MOs.

Relative ionization cross-sections by high energy electron impact ionization are proportional to pole strength values (1.0 as the maximum value), while relative band intensities in photoionization spectra are known to be nearly the same when ionization occurs from the MOs composed of the same set of atomic orbitals (AOs) [42]. Therefore, it is difficult to obtain direct experimental information on spatial electron distributions of molecular orbitals from relative band intensities in photoionization or electron impact ionization electron spectra. On the other hand, for Penning ionization electron spectroscopy, relative band intensities can be related to the spatial characteristics of MOs, because the Penning ionization process has been considered to be governed by an electron exchange mechanism (figure 4) [43, 44]. In this electron exchange mechanism, an electron in an occupied MO ϕ_j is transferred into the vacant inner-shell orbital χ_{1s} of He* and an electron is ejected into a continuum-state orbital φ_e from the occupied outer-shell orbital χ_{2s} of He*.

Since a metastable atom A* cannot penetrate into the atomic nuclear region of target molecules due to atomic nucleus repulsive interactions, an orbital exposed to the outside has a tendency to give a higher intensity in PIES bands than the case of an orbital localized in the inside. This stereoelectronic character of MOs was examined [26, 27] by relative PIES band intensities as described in section 1 with careful correction of the electron transmission efficiency of the electron spectrometer. After the general tendency of the reactivity of MOs was investigated for various inorganic and organic molecules, a repulsive boundary surface as an exclusion surface was introduced for separating the

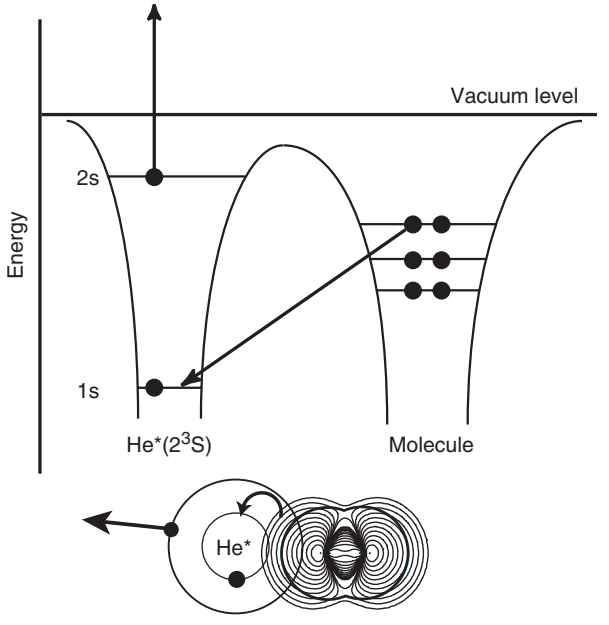

Figure 4. Electron exchange model in Penning ionization. Electron transfer from a target molecule to He* 1s orbital is followed by electron ejection from 2s orbital to vacuum.

active exterior region for the electron extracting reaction by metastable atoms A* from the inactive interior region. This model led the PIES relative band intensities to a qualitative analysis of stereoelectronic distributions of MOs extending outside the repulsive boundary surface, and EED outside the simple van der Waals surface was calculated for each MO function [26–29]. If one wants to calculate the repulsive boundary surface precisely, one may need to perform interaction potential energy calculations by *ab initio* molecular orbital methods for the excited state of He*(2^3S)–M embedded in the ionization continuum at the energy of ~20 eV with respect to the neutral ground state, which can result in a vast computational cost. Since the energy level of the 2s orbital of He* is high (ca. −4 eV) and the distribution of valence MOs is more or less anisotropic, interorbital interactions between frontier MOs of the target M and the 2s orbital are relatively strong and the potential energy surface for He*–M should be highly anisotropic. It follows that band intensities in PIES corresponding to individual ionic states of the molecule can independently change as functions of the collision energy between He* and the target molecule, which leads to varieties in collision energy dependence of partial Penning ionization cross-sections (CEDPICS) [36, 37].

2.2. *Simple calculation for reactivity of MOs depending on collision energy*

In Penning ionization, the reaction probability crucially depends on local characteristics of the electron distribution of the respective MO, and therefore the local nature of the interaction potential energy surface may be probed by metastable atoms. Since the

asymptotic decay of all MOs is directly related to the lowest ionization energy (I_0) of the target molecule [45–48] by an expression of $\exp\{-2(2I_0)^{1/2}R\}$ for the distance R, the radial dependence of the ionization width in equation (6) for all MOs should be the same. However, the reaction probability to each ionic state was found to show a difference in the collision energy dependence with the change of E_c [37]. This difference can be ascribed to the highly anisotropic interactions around the target molecule, where trajectories of the metastable atoms are deflected variously around the reactive region depending on the collision energy, the impact direction, and the impact parameter. Thus the dynamical nature of the potential energy surface can be studied with various velocity collisions of metastable atoms. In the spatial region where attractive potentials between a metastable A* and a target M govern the interaction, ionization cross-sections are expected to decrease with the increase of collision energy, because the slower He* atoms may be deflected to interact more effectively than the faster He* atoms as region (I) in figure 1. In the case of repulsive interaction region, on the other hand, ionization cross-sections are expected to increase with the increase of collision energy, because the faster He* atoms may enter into the reactive region more deeply against the potential wall, resulting in the larger overlap between relevant orbitals than the slower atoms as region (II) in figure 1. The slope parameter in a $\log\sigma - \log E_c$ plot is related to the effective hardness of the repulsive potential wall for V^* by equation (7).

A simple model calculation of exterior electron density for the j-th ionic state (EED_j) by using the anisotropic repulsive boundary surface as an exclusion surface was performed for linear molecules in order to calculate collision energy dependence of exterior electron densities (CEDEED) [49], and the obtained CEDEED curves can be compared with experimental CEDPICS. In the CEDEED calculation, the interaction potential energy was obtained by *ab initio* molecular orbital method utilizing a ground state Li atom in place of the metastable He*(2^3S) atom based on the well-known resemblance between He*(2^3S) and Li(2^2S) [50–52]. Full counter-poise (FCP) corrections [53] and the second-order Møller–Plesset perturbation calculations (MP2) were used, and contour maps of the position of the Li atom for given potential energies were obtained with the help of a simple spline program. The boundary surface for the EED calculation at various collision energies was estimated by subtracting the van der Waals radius of He (1.5 Å) from the respective closest distances determined from the Li–M interaction potentials. The EED values and partial ionization cross-sections (σ_j) for the exterior regions (EXT) outside the boundary surface of target molecules were calculated as a function of the collision energy E_c by the following equations;

$$\mathrm{EED}_j(E_c) = \int_{\mathrm{EXT}(E_c)} |\phi_j|^2 \mathrm{d}v \tag{9}$$

$$\sigma_j(E_c) = \frac{A \times \mathrm{EED}_j(E_c)}{E_c^{1/2}}, \tag{10}$$

where dv is the volume element and A is the proportionality constant. In this model, the boundary surface is completely a hard core potential which is determined by potential energy corresponding to the collision energy between He* and the target. The EED values indicate the spatial extent of electronic wave functions of target orbitals outside

the considerably changing anisotropic repulsive boundary surface with assumption of constant statistical probability in the exterior region for finding A* at a point (r, p) in the phase space defined with geometrical coordinates r of A* with respect to the target molecule, and their conjugate momenta p [27]. The square root of the collision energies in the denominator in equation (10) can be related to a correction factor of the effective interaction time for hard collisions. Dynamical aspects of various velocity collisions were partly introduced by the collision-energy-dependent EXT region as well as the interaction time factor $E_c^{-1/2}$.

Figure 5(a) shows CEDEED (dashed lines) [49], CEDPICS by trajectory calculation of He* atoms (solid lines), and observed CEDPICS obtained from 2D-PIES by the velocity-resolved technique combined to PIES (filled circles) [54]. Anisotropic interaction potential energy contour maps are also shown in figure 5(b) for C_2H_2–Li in the level of MP2 + FCP [49] and (c) for C_2H_2–He*(2^3S) utilized in the trajectory calculation [54]. Contour maps of the electron densities for molecular orbitals corresponding to the respective ionic states are also shown in figure 5(a). Observed CEDPICS for the $^2\Pi_u$ state is negative in the log $\sigma_j - \log E_c$ plot in the observed collision energy range 20–400 meV, while positive slopes of CEDPICS

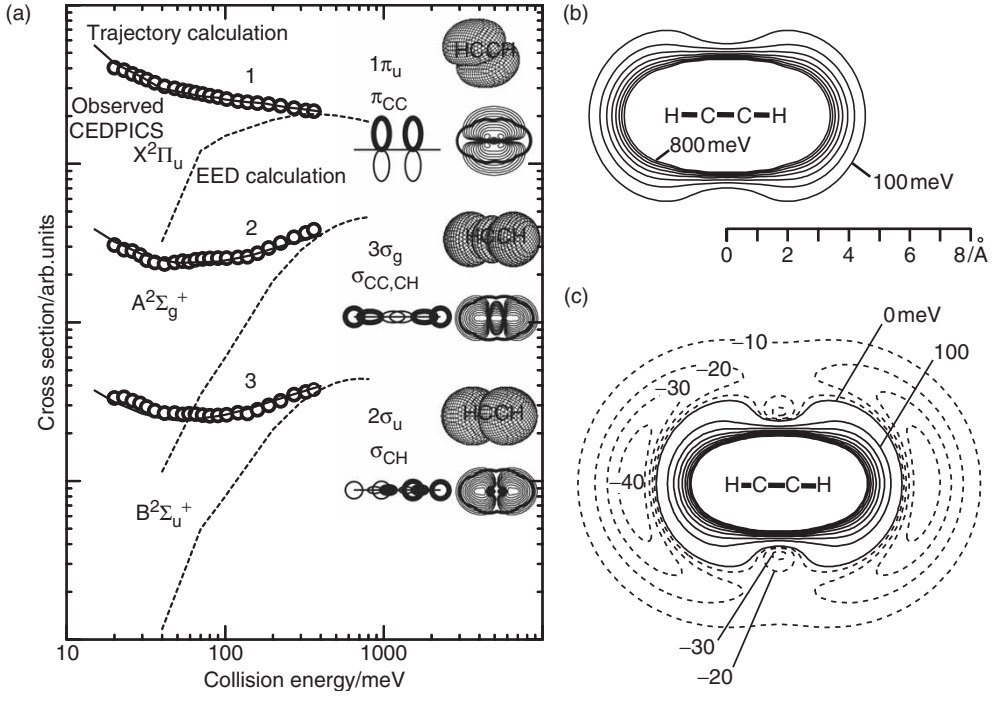

Figure 5. (a) Collision energy dependence of partial ionization cross-sections for C_2H_2 with He*(2^3S) by experiment (filled circles) and calculation with CEDEED model (dashed curves), and trajectory calculations (solid curves). Electron density contour maps and schematic representation with circles and ellipses of molecular orbitals of C_2H_2 are also shown. Potential energy contour maps for (b) C_2H_2 with Li in the level of MP2 + FCP, and (c) C_2H_2 with He*(2^3S) determined by trajectory calculation for CEDPICS. Boundary contours of the closest location of the probe atom were shown with an energy spacing of 100 meV, and negative energy lines (dashed curves) were shown with an energy spacing of 10 meV.

were observed for σ ionization at collision energy range larger than 100 meV. This difference of slope between π and σ ionization in CEDPICS in the larger collision energy range can be ascribed to a soft repulsive interaction wall around the σ_{CH} bonds rather than the π_{CC} region. The CEDEED considerably deviates from the observed CEDPICS at the lower E_c range, whereas CEDEED in the larger E_c range tends to agree with the experiments. This tendency in the larger E_c range is reasonably explained by the EED model in which relative ionization cross-sections in Penning ionization are governed by the excluding effect of repulsion between colliding particles. When two interaction potential contour maps are compared in figure 5(b) and (c), it is clear that the large deviations of CEDEED at lower collision energy regions can be ascribed to insufficient dynamical effects of He* trajectories, underestimation of attractive interaction around σ_{CH} bonds as well as the π_{CC} region, and overestimation of softness at repulsive interaction between He*(2^3S) and C_2H_2. The anisotropic interaction studied by 2D-PIES and trajectory calculations will be discussed in section 5.

3. Development of collision-energy/electron-energy-resolved two-dimensional Penning ionization electron spectroscopy

In order to achieve a simultaneous measurement of CEDPICS and CERPIES, collision-energy-/electron-energy-resolved two-dimensional Penning ionization electron spectroscopy (2D-PIES) [38] was developed with an improvement of a metastable beam source [37, 55], techniques for collision-energy-resolved measurements and continuous 2D data accumulation. A schematic diagram of highly sensitive 2D-PIES apparatus is shown in figure 6.

3.1. *Development of strong metastable atomic beam source*

Metastable atomic beam sources can be classified into an electron impact type or a gas discharge type. The metastable helium atoms produced by the electron impact type beam source has a narrow velocity distribution and are suitable for cooling to low velocity (ex. 900 m/s [56]). Generally, it is difficult to obtain large beam intensity by the electron impact method. On the other hand, the gas discharge type source can generate a strong and high temperature metastable beam because of the high electric current [57]. For the measurement of PIES, a strong metastable atom beam is required. In addition, the velocity distribution should be constant during the velocity-resolved measurements. We have developed a strong nozzle discharge source utilizing a tantalum hollow cathode and a boron nitride (BN) cap [37, 55]. Since this nozzle source was designed for discharge between the cathode and the skimmer, this source has an advantage in the collision free part outside the nozzle, which avoids large amount of de-excitation of A* due to collisions. This beam source has been stably operated, and the beam intensity is ca. 1.6×10^{15} atoms $sr^{-1} s^{-1}$ with a velocity distribution of 1500–4000 m/s. The produced He*(2^1S) component in the metastable beam can be quenched via optically allowed atomic state of He*(2^1P) by infrared light ($h\nu = 0.602$ eV) from a water-cooled helium discharge lamp [58, 59].

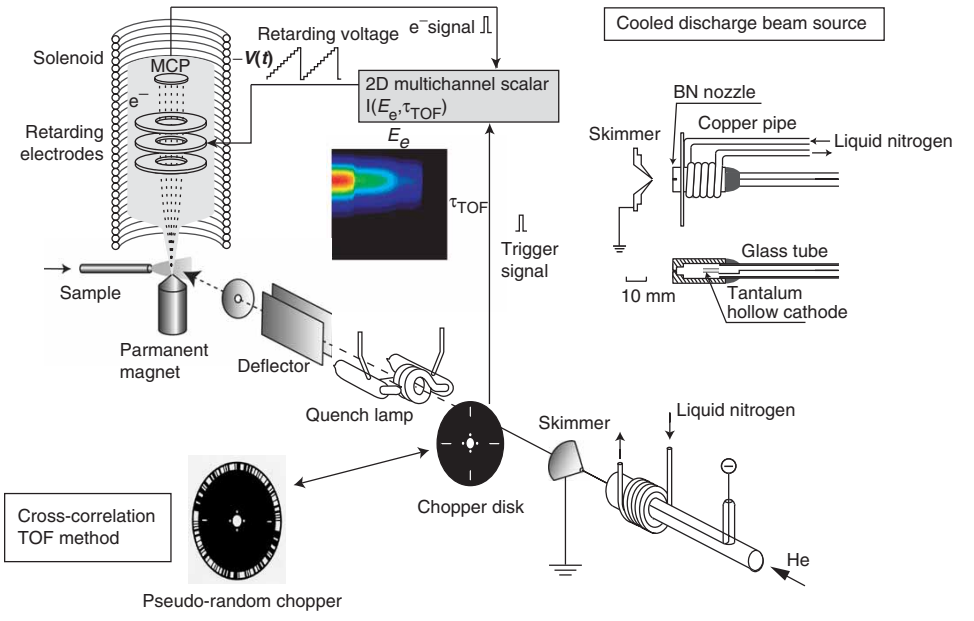

Figure 6. [Colour online] Schematic diagram of highly sensitive two-dimensional Penning ionization electron spectrometer equipped with a magnetic bottle retarding-type electron analyser. Pseudo-random chopper for a cross-correlation TOF method and a nozzle discharge source for cooled metastable beams are also shown.

In order to observe the reaction in a low collision energy range, a cooled discharge metastable beam source was developed [60]. In this method, liquid nitrogen was circulated in a copper pipe around the BN nozzle, and the mean velocity was estimated to be ca. 1300 m/s with a lowered discharge power of 6 W. The intensity of this cooled beam source is ca. 3.8×10^{14} atoms $sr^{-1} s^{-1}$, and the life time of the source is longer than 300 hours. The nozzle temperature with the liquid nitrogen circulation was estimated to be 180 K, while the estimated nozzle temperature for the normal discharge condition is 610 K [60]. This cooled discharge metastable beam source has enabled us to measure 2D-PIES in a wide collision energy range of 20–400 meV. Recently, various kinds of He metastable atomic beams of a nozzle discharge type have been developed due to the application in atom and quantum optics such as Bose–Einstein condensation (BEC) [61] and photoassociation spectroscopy [62]. In order to maintain the discharge, high currents are necessary, which results in high nozzle temperature. Appropriate coolants such as liquid nitrogen [62] or liquid helium [63] for nozzle head or holder are utilized to produce low velocity metastable beams (< 2000 m/s).

3.2. *Collision-energy-resolved technique*

The A* beam has a wide velocity distribution due to thermal energies by the discharge at the beam source, and therefore velocity (or collision energy) selection of A* is necessary for the collision-energy-resolved measurements. A conventional velocity selector reduces the number of A* atoms of a particular velocity due to several

mechanical chopper disks. Utilization of continuous time-of-flight (TOF) distributions can increase the efficiency of the collision-energy-resolved measurements by 10^3 times compared with the conventional velocity selector [40, 64]. In order to avoid the low efficiency in the velocity selection, we have adapted time-resolved measurements of the wide range of TOF signals using a four-slit chopper disk with the slit width of 2 mm. The velocity distribution of the metastable He*(2^3S) atomic beam $I_{\mathrm{He}^*}(v_{\mathrm{He}^*})$ was obtained from microsecond data accumulation of secondary electrons emitted from a stainless steel plate inserted into the collision centre. It is important to note that the time scale of the electron motion from the stainless steel plate to a detector (10^{-7} s) is negligibly shorter than the TOF of the He* atomic beam (10^{-4} s) from the chopper disk to the collision centre.

Improvement of efficiency in the TOF measurement of the metastable beam was achieved with the multiplex principle by the cross-correlation technique [65, 66]. In the cross-correlation method, the metastable beam was modulated with a pseudo-random chopper which has a slit area of approximately one half transmission for the beam, and the following Hadamard transformation of observed time-dependent spectra was used [39]. Periodic rotation of the slit pattern of the pseudo-random chopper corresponds to an N by N cyclic matrix $\boldsymbol{A}$ consisting of binary elements (unity corresponds to the passage of beam and zero corresponds to the closure of beam). Observed time-dependent spectrum $\boldsymbol{y}$ can be represented by the overlapping of the slit binary pattern depending on the metastable beam velocity distribution. When $\boldsymbol{x}$ is the TOF distribution spectrum of metastable atoms, this relation can be shown by the following equation,

$$\boldsymbol{y} = \boldsymbol{A}\boldsymbol{x}. \tag{11}$$

An inverse matrix $\boldsymbol{A}^{-1}$ can be obtained by replacing zero to minus one in the transposed matrix ($\boldsymbol{A}^{\mathbf{T}}$) of $\boldsymbol{A}$, which originates from cross-correlation of the binary sequence determined by the slit pattern. Then, the TOF spectrum $\boldsymbol{x}'$ of the metastable beam is given by the relation

$$\boldsymbol{x}' = \boldsymbol{A}^{-1}\boldsymbol{y}. \tag{12}$$

This technique employs the Hadamard transformation [67], and it is known that cyclic Hadamard matrix can be made with the number of elements $N = 2^n - 1$ ($n > 1$). Since the pseudo-random sequence consists of $(N+1)/2$ zeros and $(N-1)/2$ ones, the beam intensity is about 50% of the metastable atomic beam, while only 1% or so was used in the case of a single slit chopper. Figure 7 indicates schematic diagrams of (a) a beam modulation by a pseudo-random chopper as well as modulation matrix (Hadamard mask) determined by the slit sequence and (b) the Hadamard transformation. By the pseudo-random chopper with the slit element number N, one can achieve a better signal-to-noise ratio by $[(N+1)/2]/N^{1/2}$ times. More slit elements results in a better measurement efficiency. However, the chopper diameter is limited by the design of the vacuum chamber, and the width of one slit element must to be narrower than the beam diameter (ca. 1.0 mm) for proper beam modulation. Our pseudo-random chopper disk has a photo-etched pseudo-random pattern of 127 ($=2^7 - 1$) elements with unit slit width of 1.2 mm on a 104-mm diameter and 0.2 mm thick brass disk [39]. Finally,

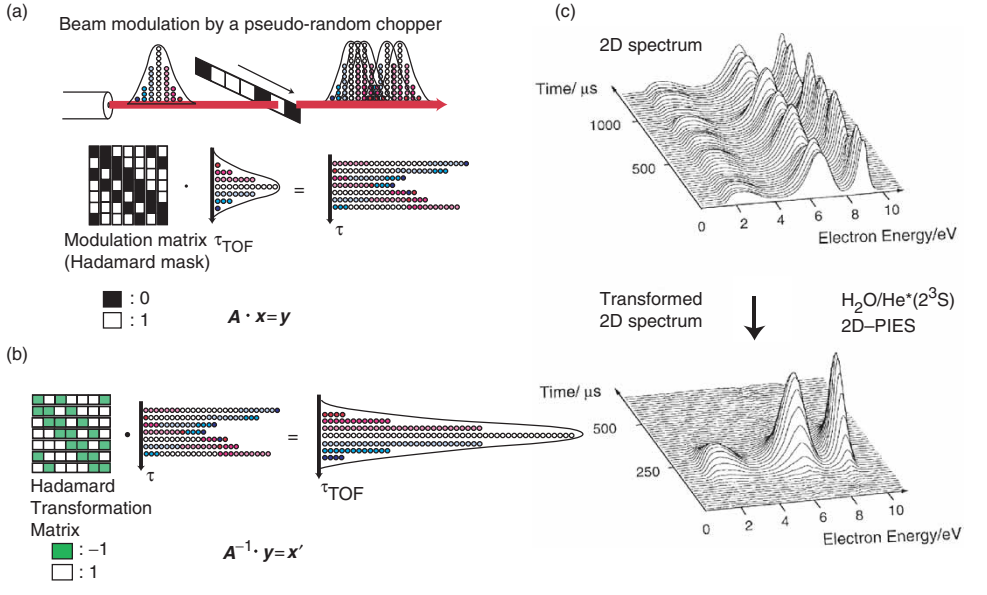

Figure 7. [Colour online] Schematic diagrams of (a) the beam modulation by a pseudo-random chopper as well as the modulation matrix (Hadamard mask) determined by the slit sequence, (b) the Hadamard transformation, (c) an observed 2D spectrum as functions of time as well as electron kinetic energy E_e, and a converted 2D spectrum.

electronic counts increased by ca. 50 times and signal-to-noise ratio got better by ca. 7 times than the case of a single slit chopper. The observed 2D spectrum as functions of time τ and electron kinetic energy E_e are shown in figure 7(c) with a converted 2D spectrum.

Resolution of the velocity measurement can be determined mainly from the chopper rotation frequency, the slit width, and the flight length. The mechanical chopper was rotated at ca. 400 Hz using a synchronous motor (Globe Motors, 18A1003-2). Estimated typical collision energy errors for the flight length of 735 mm from the chopper disk to the collision centre are around 20 meV at $E_c = 150$ meV and 5 meV at $E_c = 50$ meV for supersonic beam targets and 25 meV at $E_c = 150$ meV and 9 meV at $E_c = 50$ meV for effusive targets.

3.3. *Two-dimensional measurements of electron signals*

The first measurement of CERPIES in our group was accomplished with an electric gate to select Penning electrons with a certain range of TOF for hot (high velocity) and cold (low velocity) metastable atoms [68]. This kind of two-parameter measurements as functions of collision energy E_c and electron energy E_e by changing the detection electron energy or the delay time from a trigger signal can result in a long time accumulation or low reliability without full automatic scanning and storing in a random access memory. Thus we have developed a 2 MB two-dimensional multi-channel scalar (MCS) with Laboratory Equipment Corporation for the simultaneous measurements of

collision-energy/electron-energy-resolved PIES at a time resolution of 10^{-6} s [38, 40]. Electron energies are scanned by a step of 10 meV, and a typical dwell-time for the TOF measurement is 30 ms. In the case of cross-correlation method using a pseudo-random chopper, observed 2D data were converted by Hadamard transformation along the time axis with chopper frequency and transformation matrix determined by the chopper slit sequence. The 2D Penning ionization cross-section $\sigma(E_e, v_r)$ can be obtained from 2D data $I(E_e, v_{He^*})$ by the equations

$$\sigma(E_e, v_r) = c\left\{\frac{I(E_e, v_{He^*})}{I_{He^*}(v_{He^*})}\right\}\left(\frac{v_{He^*}}{v_r}\right) \tag{13}$$

$$v_r = \left[v_{He^*}^2 + \left(\frac{3kT}{M}\right)\right]^{1/2}, \tag{14}$$

where v_r is the relative velocity averaged over the velocity of the target molecule, k is the Boltzmann constant, and T and M are the gas temperature and the mass of the target molecule, respectively. Collision energies for the relative motion between He* and M were calculated with the reduced mass of the system μ by the equation

$$E_c = \left(\frac{1}{2}\right)\mu v_r^2. \tag{15}$$

In order to achieve considerably high sensitive electron spectroscopy in comparison to conventional hemispherical electrostatic deflection type electron energy analysers with collision cell filled by target gaseous sample, we have introduced a 4π electron collection technique using an inhomogeneous magnetic field known as the magnetic bottle effect [69, 70] into Penning ionization electron spectroscopy [71]. Almost all electrons emitted around the collision centre were collected by the strong magnetic field of 800 G together with the weak magnetic field of 6 G in a solenoid surrounding the flight tube, and they were led to a dual microchannel plate (MCP) through retarding electrodes being composed of nine metal rings for electron energy analysis. The electron energy spectra were observed by scanning the retarding field and differentiating the integrated electron signals. This magnetic bottle electron analyser has increased the electron detection efficiency of our electron spectroscopy apparatus by a factor of 10^3 and enabled us to measure Penning electrons at a 'magic angle' being independent of detection angle with respect to the metastable beam vector. Although normal hemispherical electrostatic deflection type electron energy analysers with electron lens need a correction of energy discriminations for the transmission efficiency by comparing our data with some standard spectra [72], the electron energy dependence of the discriminations was found to be almost negligible in our retarding-type electron energy analyser.

4. Theoretical calculations for stereodynamics of Penning ionization

Theories of Penning ionization for an atomic target have been established by Nakamura [16] and Miller [17, 18]. Pioneering theoretical calculations of ionization cross-sections

based on *ab initio* potential energy surface and ionization width have been made for N_2 [73] and H_2O [74], though a comparison of calculated CEDPICS with experiments showed considerable discrepancies. Semiempirical approaches have been often used for interaction potentials such as methyl halide with Ne*(^{3}P) [75] and nitrogen with He*(2^1S) [34]. *Ab initio* interaction potential energy calculations for M–A* are limited to very small molecules [73, 74, 76, 77], and model calculations based on the similarity between metastable rare gas atoms and alkali atoms [50–52] are useful as a first approximation. In order to analyse experimental data on Penning ionization, we have developed a classical trajectory method for the collisional ionization process. We will here briefly describe important aspects and application of the trajectory calculations.

4.1. *Classical trajectory calculations for collisional ionization*

Stereodynamics of heavy particle collisional ionization can be studied by classical trajectory calculations with the interaction potential V^* for the entrance channel (M + A*) and the transition probability P [78, 79]. In the classical trajectory calculations, a target molecule M has a rotational energy determined by the Boltzmann distribution at 300 K, and an impact parameter b and a collision energy E_c of a colliding atom A* are given. The transition probability $P_b(R)\mathrm{d}R$ in the interval between R and $R+\mathrm{d}R$ can be calculated with the survival probability $S_b(R)$, the transition rate $W(R)$ ($=\Gamma(R)/\hbar$), and time $\mathrm{d}t$ as

$$P_b(R)\cdot \mathrm{d}R = S_b(R)\cdot W(R)\cdot \mathrm{d}t. \tag{16}$$

The survival probability is obtained from the following equation

$$S_b(R) = 1 - \int_R^\infty P_b(R)\mathrm{d}R. \tag{17}$$

Calculations for various initial parameters with particular collision energy E_c were performed for typically 10^4 trajectories, and results were integrated to obtain ionization cross-section σ,

$$\sigma = 2\pi \int_0^\infty P_b(R) b \mathrm{d}b. \tag{18}$$

Potential data were interpolated with cubic spline functions to obtain the potential energy value at arbitrary orientation and distance. In order to obtain accurate potential energy values, we have adopted a polar coordinate cubic spline technique. In this method, spline treatments are made along radial directions at first and then along circular directions due to the complex anisotropy of molecules.

4.2. *Calculation of interaction potentials for entrance and exit channels*

The most accurate calculations of two potential functions for the entrance and exit channels are considered to be made by sophisticated *ab initio* molecular orbital methods

including electron correlation effects. However, both potential functions involve highly excited states in the full span of three-dimensional coordinates, which requires vast computational resources. In order to avoid these difficulties in potential calculations, we adopted a simple model potential by considering the essence of the interactions.

The entrance potential energy surface V^* of highly excited states ($E(\mathrm{He}^*2^3\mathrm{S}) = 19.82\,\mathrm{eV}$) embedded in ionization continuum is difficult to determine. It has been established that interaction potentials between A* and various targets can be approximated by replacing A* by the respective alkali atom, which is based on the similarity in interactions because of the same electron configuration in the valence shell. In the case of He*(2^3S), the ground state Li(2^2S) atom can be used [50–52] for the *ab initio* MO calculations to obtain a model potential V_0 as a first step as mentioned in section 2.2. The next procedure toward the accurate V^* is introducing semiempirical parameters and optimization of the model potential V_0 of Li–M, which can supplement important interorbital interactions and electron correlation effects. Although a simple scaling factor [78, 80] or exponential correction terms [81, 82] combined with V_0 were effective for linear target molecules such as N_2 and CO, the following overlap expansion (OE) method [83] was developed to be more efficient in the optimization procedures for highly anisotropic systems. In this OE method, correction terms consist of interorbital interactions between a Slater-type atomic orbital function χ at the position of the He*(Li) atom and the j-th MO ϕ_j:

$$V^*_{\mathrm{OE}} = V_0 - \sum_j C_j \left|\langle \phi_j | \chi \rangle\right|^2, \tag{19}$$

$$\chi = \sqrt{\xi^3 \pi^{-1}}\, \exp[-\xi r]. \tag{20}$$

Here, the parameters C_j and ξ should be optimized by using experimental data for the collision energy dependence of partial Penning ionization cross-sections (CEDPICS). This OE method is able to compensate the difference between He*(2^3S) and Li(2^2S) in the interaction of an s-type atomic orbital and the frontier orbitals.

The exit potential surface $V^+_{(j)}$ for the j-th ionic state can be obtained from electric configuration interaction (CI) calculations for different geometries of A–M$^+$. Since the ionization energies are limited within valence electrons in the case of Penning ionization, we have also tried to calculate $V^+_{(j)}$ by summation of the neutral potential V_{G} and the ionization energies $IE_{(j)}$ as

$$V^+_{(j)} = V_G + IE_{(j)}. \tag{21}$$

The ionization energies were obtained with outer-valence Green's function method (OVGF) [84, 85] or orbital energies based on Koopmans' theorem [86]. Utilizing both entrance and exit channel potentials, one by one electron energy calculations on the He* trajectories together with partial ionization cross-sections for various collision energies can result in 2D Penning electron spectra $\sigma(E_{\mathrm{e}}, E_{\mathrm{c}})$ except for the vibrational structure in observed spectra.

4.3. *Calculation of ionization widths*

For the ionization width Γ or the transition rate W of Penning ionization, a simple exponential function $\Gamma(R) = B\exp(-bR)$ on the distance R has been assumed in many earlier studies [13, 19, 50]. However, both B and b should be highly anisotropic for molecular targets [87]. As for molecular targets, a direct calculation of $\Gamma^{(j)}$ for N_2 showed [88] very similar R dependences to those estimated with overlap integral between a molecular orbital ϕ_j to be ionized and the He* 1s orbital ψ_{1s}, which can be explained by the approximation in the transition probability of Penning ionization. Since the ionization width can be expressed by the density of final states $\rho^{(j)}$, electronic Hamiltonian H_{el}, and Φ_0 and $\Phi^{(j)}$ electronic wave functions for the initial and the final j-th states as

$$\Gamma^{(j)} = 2\pi\rho^{(j)}\left|\left\langle\Phi_0|H_{el}|\Phi^{(j)}\right\rangle\right|^2, \tag{22}$$

the transition rate is approximated in terms of a product of two overlap integrals $\langle\phi_j|\psi_{1s}\rangle$ and $\langle\psi_{2s}|\phi_\varepsilon\rangle$ with 2s orbital of He* ψ_{2s} and the ejected electron orbital ϕ_ε via Slater determinant wave functions with one-electron orbitals [89];

$$\left\langle\Phi_0|H_{el}|\Phi^{(j)}\right\rangle \approx \left\langle\psi_{2s}(1)\phi_j(2)|r_{12}^{-1}|\psi_{1s}(1)\phi_\varepsilon(2)\right\rangle - \left\langle\psi_{2s}(1)\phi_j(2)|r_{12}^{-1}|\phi_\varepsilon(1)\psi_{1s}(2)\right\rangle. \tag{23}$$

The first two-electron integral vanishes for triplet helium because of spin inversion, and the second one leads to a product of two overlap integrals based on Mulliken approximation [90] for the two-electron integral $\langle st|uv\rangle$,

$$\langle st|uv\rangle = \left(\frac{1}{4}\right)\langle s|u\rangle\langle t|v\rangle\{\langle ss|tt\rangle + \langle ss|vv\rangle + \langle uu|tt\rangle + \langle uu|vv\rangle\}. \tag{24}$$

Such an approximation has been used in semiempirical MO theories as well as in semiempirical treatments for electron transfer rates [91, 92]. The overlap integral $\langle\psi_{2s}|\phi_\varepsilon\rangle$ for the electron number one indicates diffuse electron ejection function, while anisotropy of the ionization width is mainly governed by the overlap integral $\langle\phi_j|\psi_{1s}\rangle$ for the electron number two. Finally, the approximated form of the ionization width is

$$\Gamma^{(j)} \approx K^{(j)}\left|\left\langle\phi_j|\psi_{1s}\right\rangle\right|^2. \tag{25}$$

where $K^{(j)}$ can be determined in order to reproduce observed ratio or absolute values of ionization cross-sections. In connection with ionization width, two kinds of functions (MO functions and electron ejection functions) described below can be calculated via optimization of procedures as shown in section 7.

(a) *MO functions* [93]. Since the Penning ionization probability is sensitive to the electron distribution of the MO to be ionized, calculated ionization cross-sections depend on the shape of the MO function. Starting from SCF

(self-consistent field) MOs by minimal basis functions (STO-6G) for valence electrons, LCAO (linear combination of atomic orbitals) coefficients and atomic orbital exponents for valence components can be optimized by a non-linear least squares method so as to minimize the residue between observed and calculated CEDPICS curves as well as the branching ratios.

(b) *Electron ejection functions* [94]. When an electron ejection direction γ is considered, the ionization width $\Gamma^{(j)}$ can be divided into an angular factor and the rest as

$$\Gamma^{(j)} \propto \left[\sum_l Y_{lm}(\gamma) i^{-l} \exp(i\lambda_l)\right]^2 \left|\langle \phi_j \mid \Psi_{1s}\rangle\right|^2, \tag{26}$$

where Y_{lm} are spherical harmonics and λ_l is a phase shift between partial waves. Utilizing the Legendre expansions to the second term for the spherical harmonics functions with magnetic quantum number $m=0$, the angular-dependent partial ionization width can be expressed with γ, difference of phase shift ω_j, and relative intensity ζ_j between s-wave (p_0) and p-wave (p_1) as

$$\Gamma^{(j)}(\gamma) = (1 + 2\zeta_j \cos\omega_j \cos\gamma + \zeta_j^2 \cos^2\gamma) K^{(j)} \left|\langle \phi_j \mid \Psi_{1s}\rangle\right|^2, \tag{27}$$

$$\zeta_j = \frac{p_1}{p_0} \tag{28}$$

$$\omega_j = \lambda_1 - \lambda_0 - \frac{\pi}{2}. \tag{29}$$

5. Anisotropic interactions and stereodynamics of collisional ionization studied by 2D-PIES and trajectory calculations

Although positive and negative collision energy dependences of total ionization cross-sections were measured for target atoms Ar [95–98] and Hg [95, 99], respectively, anisotropic interactions around target molecules with a metastable He*(2^3S) atom have been studied with an ionic-state-resolved technique combined with a collision-energy-resolved method. Two-dimensional Penning ionization electron spectroscopy (2D-PIES) developed by our group made it possible to measure continuous electron counts as functions of two important parameters, the electron energy (E_e) and the collision energy (E_c).

5.1. *Anisotropic repulsive interactions studied by 2D-PIES and trajectory calculations*

A comparison of 2D-PIES by observation and trajectory calculations enables us to determine anisotropic interaction potentials V^* of M + He*(2^3S) by optimization of the parameters. Figure 8 shows (a) observed and (b) calculated 2D-PIES for N_2 + He*(2^3S) [82, 100, 101]. The collision-energy-resolved PIES for $E_c = 100$ meV and 300 meV were also shown in the right-hand panels. Vibrational structures were constructed by

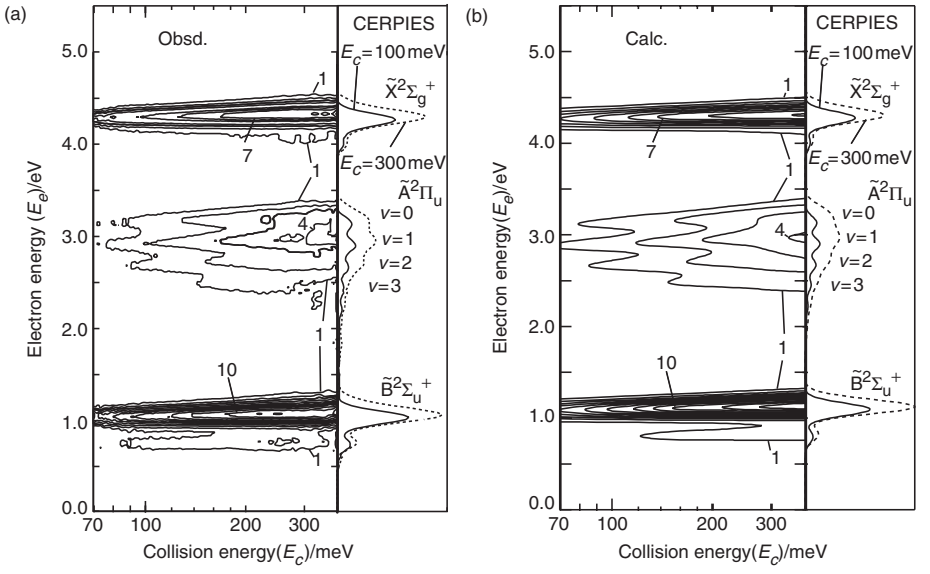

Figure 8. (a) Observed and (b) calculated two-dimensional Penning ionization electron spectra (2D-PIES) for $N_2 + He^*(2^3S)$. The right hand panel shows CERPIES for collision energies of 100 (solid line) and 300 (dashed line) meV.

distributing ionization probabilities according to the Franck–Condon factors and vibrational frequencies [102]. The calculated peak positions are in good agreement with the observed values within 10–60 meV. The peak position was found to be insensitive to the exit potentials for $N_2 + He^*$; even if the exit potentials are artificially replaced by a completely flat potential, the calculated peak position coincide within 10 meV reflecting compressed repulsive wall in the exit channels to the shorter distance in comparison with the entrance channel [82].

The parameters in the model potential were optimized by utilizing the 2D-PIES data in collision energy range from 90 to 350 meV. Figure 9 shows log σ_j vs. log E_c plots of CEDPICS for $He^*(2^3S) + (N_2, CO)$ [83]. Observed ionization cross-sections are plotted with circles, and they are compared with those by trajectory calculation results (curves). The thick solid line in the electron density maps indicates the contour curve of interaction potential of 800 meV as a reference of the repulsive boundary surface. The thick arrow indicates important directions of the ionization by collision of $He^*(2^3S)$ to the target M. The most reactive direction for π ionization is perpendicular direction with respect to the molecular axis, while collinear directions for σ ionization are shown by arrows reflecting the respective MO electron density distributions. Since total cross-sections for N_2 and CO with $He^*(2^3S)$ were normalized with crossed-beam experiments [98]. The slope of CEDPICS for the $^2\Pi$ state (filled circles) is most steeply increasing with the increase of collision energy, which indicates that the interaction potential surface is softer for side-on collisions rather than head-on collisions. It is of note that for the $A^2\Pi_u$ state of N_2, the most reactive directions change from ca. 50° to 90° from the molecular axis on going from 100 to 400 meV in collision energy [78]. This unusual behaviour is related to the dramatic change of the outer shape of the boundary surface

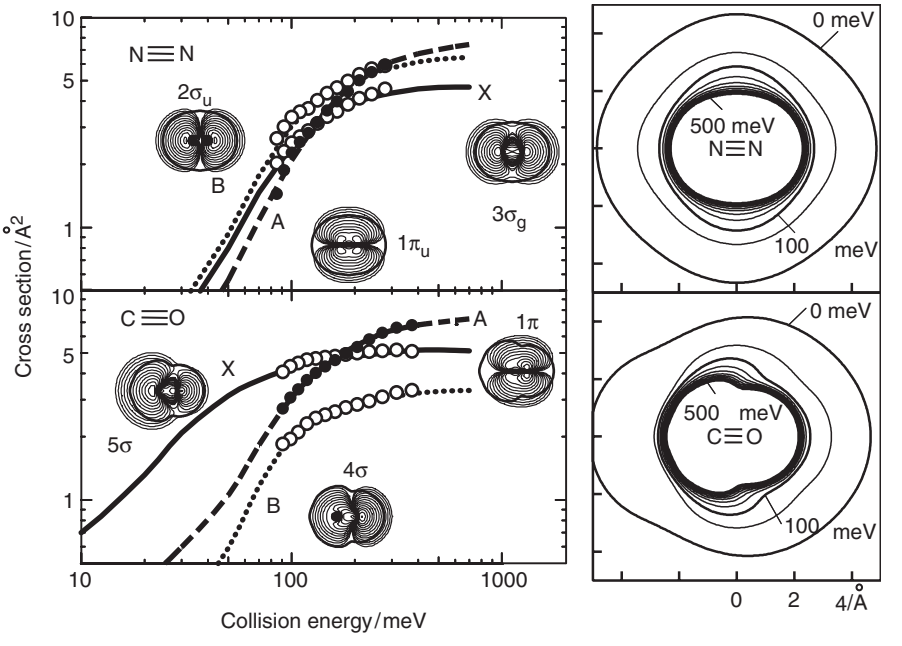

Figure 9. CEDPICS for He*(2^3S) + (N_2, CO) by experiments (circles) as well as trajectory calculations (curves). Contour maps of electron densities for MOs corresponding to the respective ionic states are also shown.

for N_2 with He*(2^3S) from the oblate form to the prolate form with increasing energies. The observed CEDPICS for two types of $^2\sum$ states (open circles) are nearly the same for N_2 because of similar electron distributions of $3\sigma_g$ and $2\sigma_u$ orbitals in the collinear directions, while anisotropy was observed for ionization from 5σ and 4σ orbitals of CO (open circles) due to the harder repulsive interaction potential for head-on collision to the carbon side than that for oxygen side.

Optimized $K^{(j)}$ values in equation (25) showed an increasing trend as the electron energy E_e decreases [82, 83], which can be related to a factor of $2\pi\rho^{(j)}$ in equation (22) for the fundamental equation of the ionization width. When one expands outgoing electron wave functions into partial waves, this factor is normalized as $2\pi\rho^{(j)} = 4(2E_e)^{-1/2}$ in a previous paper [103]. Moreover, the energy gap between the He 1s orbital and the target ionized orbital may be responsible for this tendency in connection with electron exchange matrix elements [82, 83]. Figure 10 indicates the calculated reaction probability maps determined from trajectory calculation of CEDPICS for N_2/He*(2^3S) [83] including $K^{(j)}$ ratio of $K^{(X)} : K^{(A)} : K^{(B)} = 1.00 : 1.18 : 2.17$. They show different ionization probability distributions for individual ionic state at a given collision energy. Ionization from σ-type MOs has high possibility around the both ends of the molecular axis, while ionization from the π-type MO occurs at the perpendicular directions to the molecular axis. With the increase of collision energy, the minimum distance from N_2 to He*(2^3S) becomes shorter and the reaction probability increases.

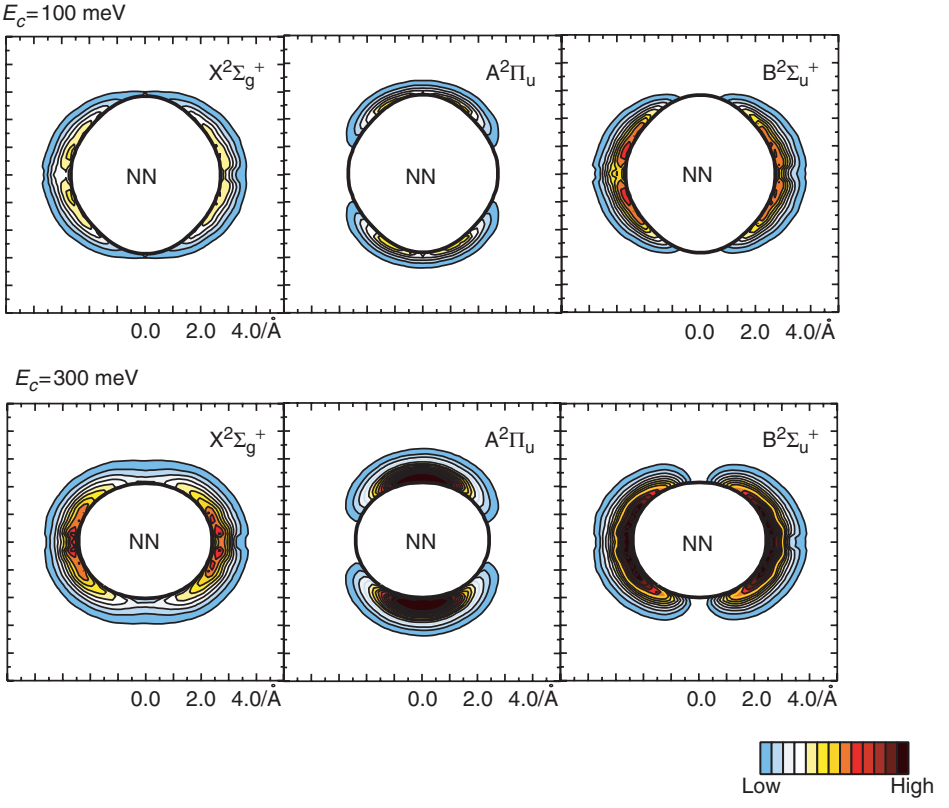

Figure 10. [Colour online] Reaction probability contour maps for the three ionic states of N_2 by collision with He* at collision energy $E_c = 100$ and 300 meV. The dark colours indicate ionization probabilities obtained from trajectory calculations. The thick solid line represents the boundary surface for the respective collision energy.

5.2. *Anisotropic attractive interactions studied by 2D-PIES and trajectory calculations*

Since observed data in the lower collision energy range are important for attractively interacting systems, CEDPICS curves in a wide collision energy range were applied to consistently determine an anisotropic interaction potential surface including an attractive interaction well. Figure 11 shows (a) observed and theoretical CEDPICS for $CH_3CN + He^*(2^3S)$ [105] as well as (b) obtained interaction potential energy curves of V_0 (CH_3CN–Li) by Li-model potential and V_{OE} (CH_3CN–He*) by the overlap expansion method [83]. As mentioned for equation (3), a negative collision energy dependence of the ionization cross-section can be ascribed to attractive interactions around the potential well in the entrance surface. The largest negative slope for the A^2A_1 state is clearly related to the deep potential well around the N-atom end of the CN group where the 'lone-pair' $7a_1(n_N)$ orbital distributes. A deep attractive well was found in the direction of the CN group with the well depth of 423 meV (~10 kcal/mol) for V_{OE}. The second largest negative slope of X^2E state also can be ascribed to an

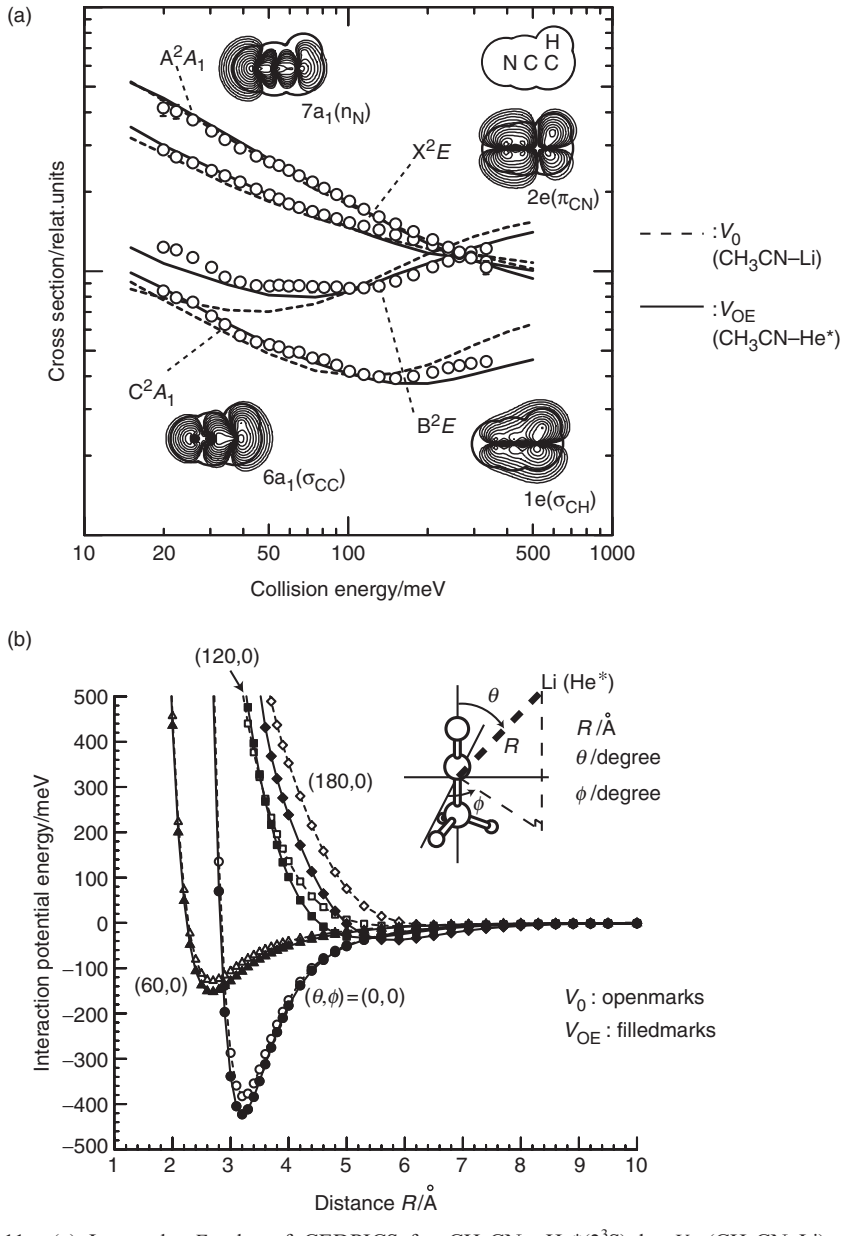

Figure 11. (a) Log$\sigma - \log E_c$ plot of CEDPICS for $CH_3CN + He^*(2^3S)$ by V_0 (CH_3CN–Li) and V_{OE} (CH_3CN–He*), and (b) interaction potential energy curves of V_0 (open marks) and V_{OE} (filled marks).

attractive interaction around the CN group, since the electron density of the corresponding 2e(π_{CN}) orbital distributes around the attractive region. The steep repulsive slope of the potential energy surface V_{OE} (He*) around the methyl group rather than V_0 (Li) results in smaller positive CEDPICS of B^2E and C^2A_1 states at the

higher collision energy region. A weak attractive well with a depth of 38 meV (~0.9 kcal/mol) was also found around the methyl group, which can be related to negative CEDPICS for B^2E state in the low collision energy region.

Highly anisotropic attractive interaction potential wells around two hetero atoms were obtained for OCS-He*(2^3S) [104] with the overlap expansion method as shown in figure 12(a). Different directions of attractive interaction were found for the collinear (head-on) direction of the C=O axis with the well depth of 90 meV and for the perpendicular (side-on) direction to the C=S axis with the depth of 40 meV, which can be ascribed to the large negative slope of CEDPICS for $X^2\Pi(3\pi, O_{2p}\text{-}S_{3p})$ and $C^2\sum^+$ (8σ, σ_{CO}) states. Calculated ionization probability distributions (opacity functions) for various trajectories and molecular orientations as a function of impact parameter are shown in figure 12(b) for $X^2\Pi(3\pi)$ and $C^2\sum^+$ (8σ) states at four collision energies ($E_c = 20$ and 300 meV). An almost constant upper boundary of the probability was obtained for impact parameters less than the critical impact parameter b_c (shown by arrows in the figure) regardless of E_c, and the critical impact parameter b_c decreases with the increase of collision energy. The negative CEDPICS for ionization from 3π and 8σ orbitals governed by attractive interaction can be related to the decreasing b_c value with the increase of E_c. Since the sum of partial ionization probabilities for each trajectory cannot exceed the unity, the constant upper boundary can be ascribed to extension of other MOs around the S atom (2π and 9σ) and O atom (9σ). On the other hand, the large number of trajectories at small probability in the opacity functions (ca. 0.05 for $X^2\Pi$ and 0.1 for $C^2\sum^+$) can be attributed to ionization at small components of 3π and 8σ orbitals around O and S atoms, respectively.

Anisotropic interaction potential energy surfaces of unsaturated hydrocarbons such as C_6H_6 [106], C_2H_2 and C_2H_4 [54] with He*(2^3S) were also consistently determined by CEDPICS and optimization by the overlap expansion method. Relatively large interactions around the π orbital regions result in negative slopes of CEDPICS for π bands, while wide small attractive well depths from 10 to 50 meV and soft repulsive interactions around the σ_{CH} regions cause a bent shape of CEDPICS with a positive slope in the higher collision energy region and a negative slope in the lower collision energy region as shown in figure 5(a) for C_2H_2–He*(2^3S). The determined interaction potential energy surface for C_2H_2–He*(2^3S) was shown in figure 5(c).

Slope values of CEDPICS were found to be changed for supersonic molecular beam targets compared with effusive target gas condition, which was investigated for CH_3CN and C_6H_6 [107]. The observed CEDPICS in the supersonic jet condition changed to the steeper positive or negative slopes for CH_3CN and the less negative for π ionization and the more positive slopes for σ ionization in the case of C_6H_6. It is known that molecules in supersonic jet with the lighter carrier gas such as H_2 and He can be aligned to some extent in order to reduce collisional cross-sections with respect to the stream of the carrier gas [108–110]. The change of CEDPICS for CH_3CN and C_6H_6 was concluded to be induced by the reduced random orientations (or distorted orientations) due to huge numbers of collisions of carrier He atoms, and our experiment was the first study by collisional ionization electron spectroscopy [107]. Steric effects upon collisional ionization between metastable atoms and oriented molecular beam have been studied directly by using an electric hexapole state-selector [111, 112].

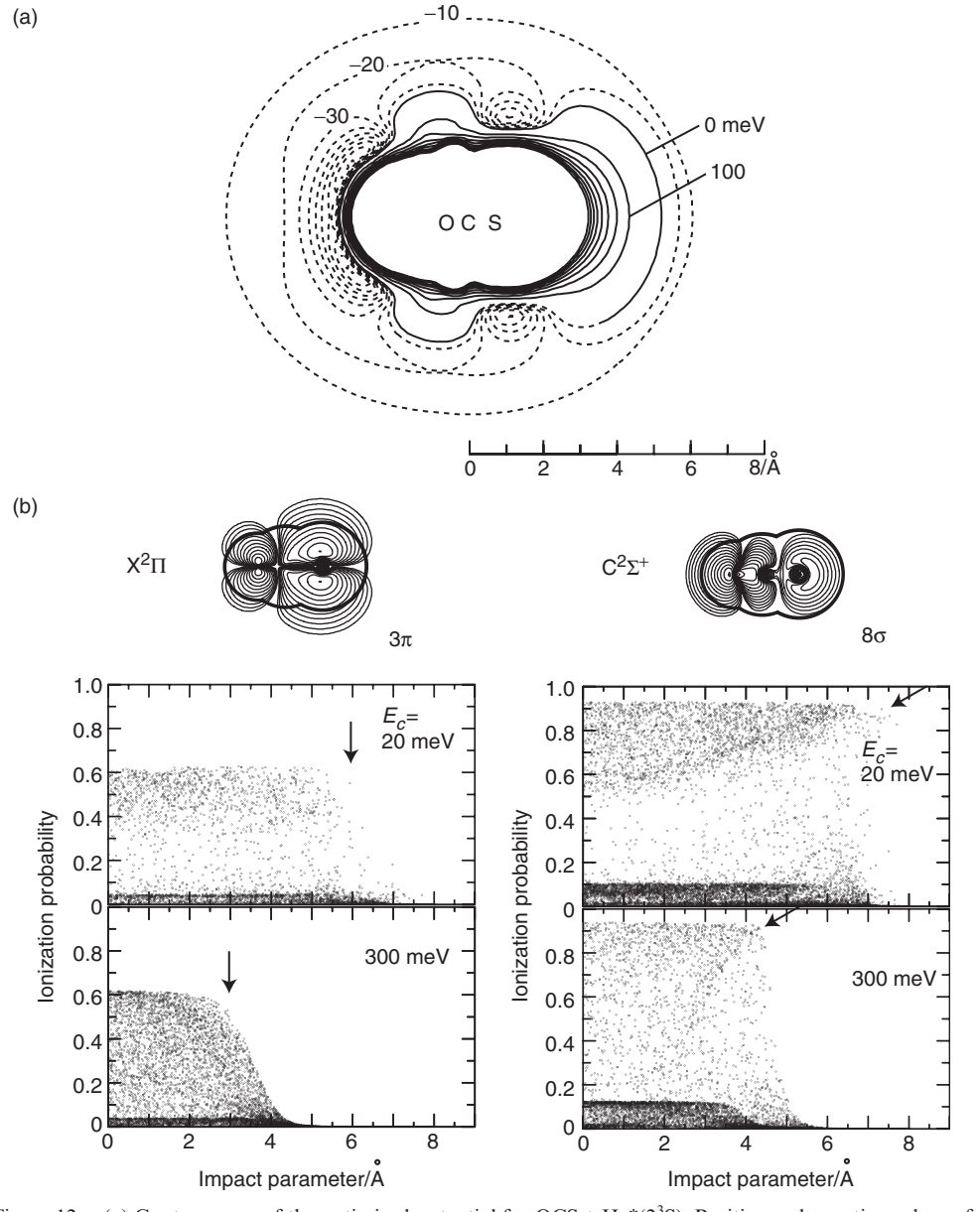

Figure 12. (a) Contour map of the optimized potential for OCS + He*(2^3S). Positive and negative values of the potential energy are shown with solid lines (from 0 to 800 meV) and dotted lines (from −10 to −80 meV), respectively, and (b) ionization probabilities as a function of impact parameter b at $E_c = 20$ and 300 meV for $X^2\Pi(3\pi)$ and $C^2\Sigma^+$ (8σ) states and respective MOs. Critical impact parameter b_c of the upper boundary is shown by arrows.

6. Electronic structure and ionization process of molecules studied by 2D-PIES

Since the first CEDPICS of H_2O, H_2S as well as O_2 was presented [36], electronic structures and ionization processes including autoionization via superexcited states or shake-up excitation have been studied based on observed CEDPICS for various target molecules.

6.1. *Attractive interaction around lone pair electrons with He* observed by 2D-PIES*

Negative collision energy dependence of the total ionization cross-section was observed for $H_2O + He^*(2^3S)$ by crossed molecular beam [113]. Although attractive interactions were found for the lone pair electron region around the oxygen atom for H_2O with He* by *ab initio* MO calculations, it was difficult to estimate the interaction well depth only from the observed negative peak energy shift with respect to nominal energy due to overlapping vibrational peaks in $He^*(2^3S)$ PIES [76]. Ionization from lone pair orbitals can show strong intensity in $He^*(2^3S)$ PIES because of the large extent of the electron density. One of the typical cases of this strong intensity in PIES bands is nitriles (R–C ≡ N) [114] that have a large dipole moment. As shown for CH_3CN in section 5.2, a large negative slope of CEDPICS was observed for ionization from n_N (σ_{CN}) orbital of acetonitrile. Similarly, a large negative slope of CEDPICS was obtained for nitriles with various groups such as propionitrile (C_2H_5CN) [39], cyanocyclopropane (C_3H_5CN) [115], CH_3SCN [116], BrCN [117], and cyanomethyl halides (CH_2BrCN [118] and CH_2ClCN [119]). The attractive interaction can be connected to polarity of the functional group, and the nitrile group has electric dipole $C^{\delta+}N^{\delta-}$ due to the larger electron negativity of an N atom than a C atom. When attractive interaction around the –NC group of methyl isocyanide (CH_3NC) was compared with –CN group of acetonitrile (CH_3CN), the weaker attractive interaction was found around the $-N^{\delta-}C^{\delta+}$ group rather than $-C^{\delta+}N^{\delta-}$ group [120], which means that the electron negative terminal is favourable for He*(Li) atoms. In addition, when two equivalent CN groups are in one molecule with opposite directions (NCCN) [121], attractive interactions around the CN groups became weak and repulsive interactions were found for perpendicular direction of the molecular axis. A contour map of electron density difference ($\Delta\rho = \rho(\text{M–Li}) - \rho(\text{M}) - \rho(\text{Li})$) for the access of He*(Li) to the CN group indicates that a large increase of electron density and polarization is caused on the Li atom (figure 13), which is different from the electron back donation from Li to acrylonitrile ($CH_2 = CHCN$) through π^*_{CC}-type LUMO (the lowest unoccupied molecular orbital) that is energetically lowered by the inductively electron-withdrawing effect by nitrile group in the conjugating system [39]. Negative CEDPICS by the attractive interaction around the π_{CC} group of acrylonitrile ($m = -0.30$) was changed to be weak (π_{CC}, $m = -0.10$) when the conjugation was interrupted by a methylene group in 3-butenenitrile ($CH_2 = CHCH_2CN$) as shown in figure 13. Large intensities in $He^*(2^3S)$ PIES bands associated with strong attractive interactions were also found for –C≡O lone-pair electrons in organometallic compounds such as (η^5–C_5H_5)$Mn(CO)_3$ and (η^6–C_6H_6)$Cr(CO)_3$ [122].

Attractive interactions around lone-pair electron regions were found for alcohols (R–OH), amines (R–NH_2), and thioalcohols (R–SH). As for anisotropy around the

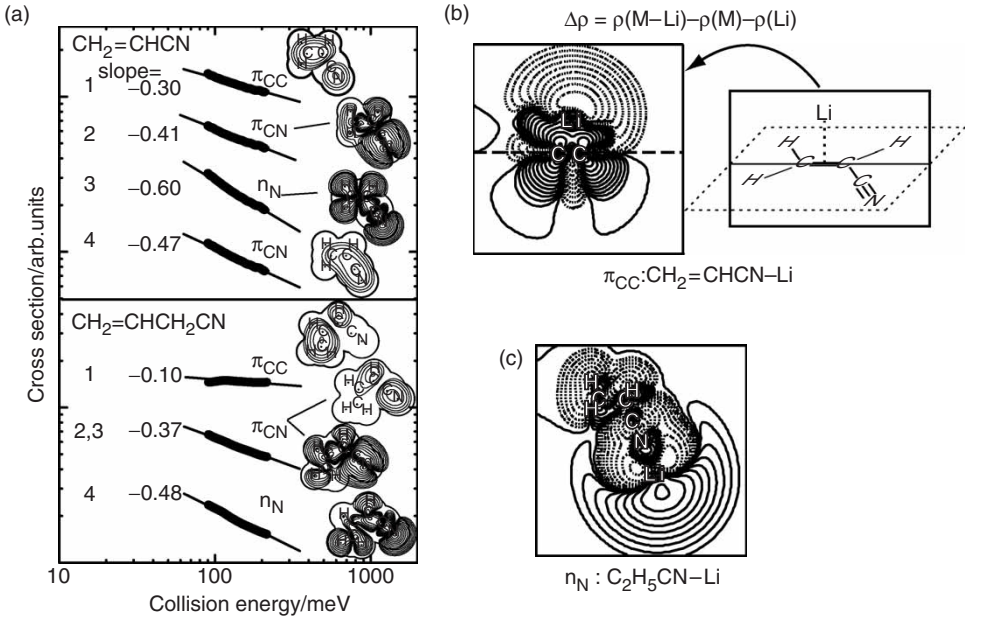

Figure 13. (a) CEDPICS for acrylonitrile and 3-butenenitrile by collision with He*(2^3S), and electron density difference maps of (b) in-plane access of Li along the CN axis of propionitrile and (c) out-of-plane access to the vinyl group of acrylonitrile ($R = 2.0$ Å). The increase and decrease of electron density is shown by solid and dashed lines, respectively. The n-th solid line from the outside is $2^{n-2} \times 10^{-5}$ au^{-3} except that $d_1 = 0$.

oxygen atom, in-plane direction is most attractive, which has been confirmed with various alcohols as well as ethers such as methanol (CH_3OH) [123], ethanol (C_2H_5OH) [124], cyclohexanol ($C_6H_{11}OH$) [125], 1-adamantanol ($C_{10}H_{15}OH$) [126], and ethers with alkyl groups ($(CH_3)_2O$, $(C_2H_5)_2O$)) [123] or cyclic ethers ($C_5H_{10}O$, C_4H_8O, $C_4H_8O_2$) [126]. Calculated interaction well depth values around the nitrogen lone pair electrons of cyclopropylamine ($C_3H_5NH_2$) [115] and ethylamine ($C_2H_5NH_2$) [127] with Li were about 400 meV and 600 meV, respectively, which is comparable to the deep well depth for in-plane access of Li to the oxygen of alcohols. For the lone pair electrons of NH_2 and OH groups, ionization cross-sections, negative peak energy shifts, and negative CEDPICS were found to be not as large as those of CN groups in comparative study of $NH_2C_2H_4CN$ and HOC_2H_4CN [127]. Intramolecular hydrogen bonding of OH...N and NH...O types was studied for 2-aminoethanol ($NH_2C_2H_4OH$), *N*-methyl-2-aminoethanol ($NH(CH_3)C_2H_4OH$), and 2-methoxy-*N*-methylethylamine ($NH(CH_3)C_2H_4OCH_3$) [128]. The hydrogen bonding effects were observed as the weak band intensity, the small peak energy shift, and the less negative CEDPICS for ionization from relevant lone pair orbitals. Anisotropic attractive interactions around the lone pair or nonbonding electrons of thioalcohols (R–SH) are quite different from alcohols (R–OH) as mentioned for OCS + He*(2^3S) [104, 129] in section 5.2. Out-of-plane directions around the sulfur atom are found to be more attractive than the in-plane direction as studied for ethyl thioalcohol (C_2H_5SH) as well as thioether

(CH_3SCH_3) or disulfide (CH_3SSCH_3) [124]. Comparative 2D-PIES study of phenol (C_6H_5OH), aniline ($C_6H_5NH_2$), and thiophenol (C_6H_5SH) confirmed the interesting difference in anisotropic interactions around the hetero atoms of functional groups including hydrogen [130].

Similar to the cases of OH and SH groups, anisotropy in interaction with He* has been studied comparatively for carbonyl (R–CO) and thiocarbonyl (R–CS) compounds such as ureas ($(NH_2)_2CO$, $(NH_2)_2CS$) [131], amides (CH_3CONH_2, CH_3CSNH_2) [132], and isocyanates (HNCO and HNCS or CH_3NCO and CH_3NCS) [116, 133]. Associated with the strong attractive interaction for collinear direction of C=O axis, the large intensity in PIES was observed for ionization from σ_{CO} orbitals of carbonyl compounds such as formaldehyde (HCHO) [134], acrolein (CH_2=CHCHO) [134], cyclohexanone ($C_6H_{10}O$) [125], while weak attractive or repulsive interactions were found for out-of-plane directions of formamide ($HCONH_2$) and acetamide (CH_3CONH_2) [132]. In the case of thiocarbonyl compounds, strong bands for ionization from S_{3p} (n_S) orbitals showed negative CEDPICS, and vertical directions to C=S axis were found to be most attractive for thiourea ($(NH_2)_2CS$) [131] and thioacetamide (CH_3CSNH_2) [132] as illustrated in figure 14(a). It is interesting that attractive interactions around the hydroxyl oxygen or amino nitrogen become considerably weak when they are included in one molecule with carbonyl or thiocarbonyl group as studied in amides, thioamides [131, 132], acids (HCOOH, CH_3COOH) [135], and methyl formate ($HCOOCH_3$) [135].

As for the negative slope of CEDPICS for ionization from π orbitals, a good correlation between the negative slope values and orbital energies of π-type HOMO (the highest occupied molecular orbital) in the order of $C_2H_4 < C_2H_3Cl < C_2H_3CH_3 < C_2H_3OCH_3$ was found [136]. The energy levels of HOMO for these compounds can be related to the degree of the electron donation from the substituent, and the π-type HOMO with the higher energy level can interact with 2s-2p orbitals of He* more effectively. Attractive interactions around the HOMO were also possible to explain interorbital interactions between the S_{3p} orbital of thiocarbonyl compounds and the 2s-2p orbitals of He*, while the sp hybridization was induced on He* due to the strong bond dipole of the carbonyl ($C^{\delta+}O^{\delta-}$) or nitrile ($C^{\delta+}N^{\delta-}$) group, and the attractive interaction was found for the collinear side of the bond [40, 104] as illustrated in figure 14(b). The polarity of the functional group was found to be important, since the attractive interaction around the $-N^{\delta-}C^{\delta+}$ group of methyl isocyanide (CH_3NC) was weaker than that of $-C^{\delta+}N^{\delta-}$ group for acetonitrile (CH_3CN) [116].

6.2. *2D-PIES study of halides by collision with He* metastable atoms*

Lone pair electrons of pseudohalides play an important role for attractive interactions around the oxygen atom of fulminic acid (HCNO) and the imine type nitrogen atom of hydrazoic acid (HNNN), and attractive interaction around 300 meV was calculated with Li [137]. In the case of halides, attractive interactions around lone pair electrons were calculated for alkyl halides R–X (C_2H_5F [138], 1-$C_{10}H_{15}Cl$ [139], $C_6H_{11}Cl$ [139], 1-$C_{10}H_{15}Br$ [140], and $C_6H_{11}Br$ [140]) with the well depth of 200 meV or more. Similarly to the case of carbonyl and thiocarbonyl compounds, anisotropic interaction around the C–X axis depends on the row of halogen atoms; the collinear direction of C–F axis and the perpendicular direction of the C–Cl or C–Br axis are the

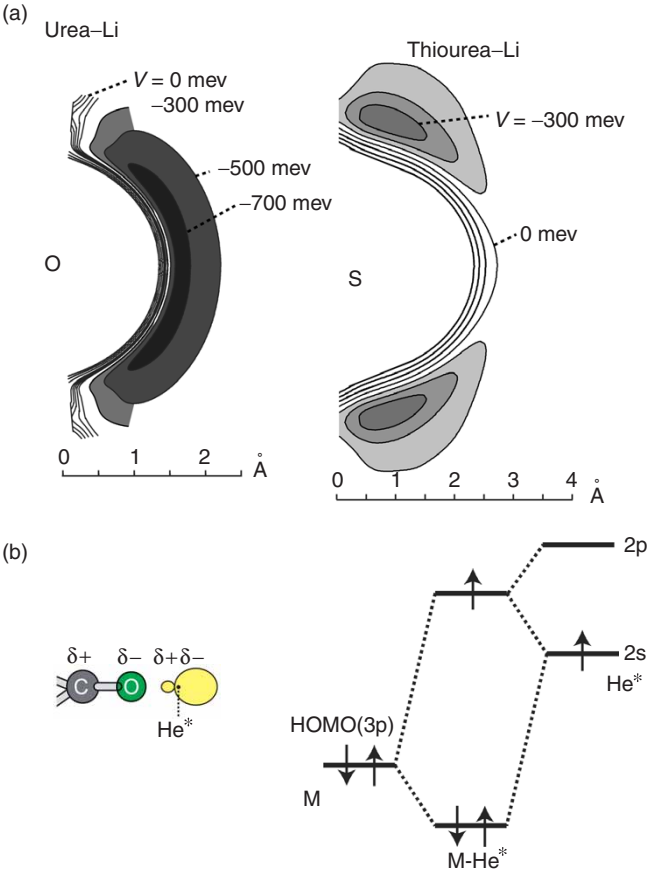

Figure 14. [Colour online] (a) Contour maps of interaction potential for urea–Li as well as thiourea–Li, and (b) sp hybridization on a He*(2^3S) atom induced by strong bond dipole of a carbonyl group ($C^{\delta+}O^{\delta-}$), and orbital interactions between 3p HOMO of a molecule M and 2s-2p orbitals of a He*(2^3S) atom.

most attractive [138–140]. In the case of CH_3Cl, off-axis directions of C–Cl were shown to be attractive both by semiempirical [75] and *ab initio* Li model [141] calculations.

When anisotropic interactions around the halogen atoms are calculated for unsaturated hydrocarbon halides such as monohalogenobenzenes (C_6H_5X) [142] and vinyl chloride (CH_2=CHCl) [143, 144], attractive well depth for collinear or vertical access to the halogen atoms for in-plane and out-of-plane directions was less than 200 meV. Negative slope values of CEDPICS for ionization from σ_{CF} MOs of fluorobenzenes (C_6H_5F [142], *o, m, p*-$C_6H_4F_2$ [145], $C_6H_3F_3$, and C_6F_6 [146]) were not so large as that of C_2H_5F ($m = -0.46 \pm 0.04$), and obtained well depth of Li model potential for C_6H_5F ($\sim$100 meV) was much smaller than that for C_2H_5F ($\sim$230 meV). The reactivity of $n_{F//}$ and σ_{CF} MOs was found to increase with the number of F atoms as $C_6H_5F < C_6H_4F_2 < C_6H_3F_3 < C_6F_6$, while the magnitude of attractive interaction around the F atoms is affected by wide attractive interaction region with neighbouring F atoms (*o*-$C_6H_4F_2$ > *m*-$C_6H_4F_2 \sim$ *p*-$C_6H_4F_2$) [145]. Figure 15 indicates CEDPICS for

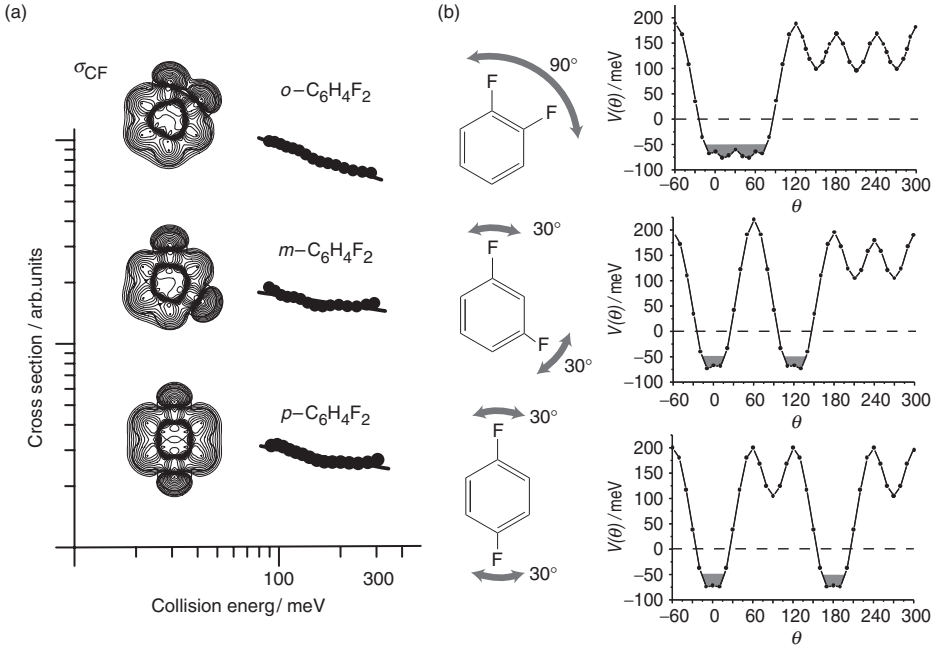

Figure 15. (a) CEDPICS for σ_{CF} MOs of *o*, *m*, *p*-$C_6H_4F_2$ by collision with He*(2^3S), and (b) interaction potential energy curves of *o*, *m*, *p*-$C_6H_4F_2$ around the F atoms. Attractive interaction regions ($V < -50$ meV) were painted, and the effective angle of 90° for *o*-$C_6H_4F_2$ and 60 (=30 + 30)° for *m*, *p*-$C_6H_4F_2$ were also shown.

ionization from σ_{CF} MOs of *o*, *m*, *p*-$C_6H_4F_2$ and interaction potential energy curves of *o*, *m*, *p*-$C_6H_4F_2$ around the F atoms [145]. Deep interaction potential well regions ($V < -50$ meV) were painted in the figure, and the effective angle results in 90° for *o*-$C_6H_4F_2$, while smaller angle of 60 (=30 + 30)° was effective for *m*, *p*-$C_6H_4F_2$.

In the case of chlorides, CEDPICS for n_{Cl} MOs show smaller slope values due to repulsive interactions by the neighbouring hydrogen atoms in $C_{10}H_{15}Cl$ ($m = -0.23 \pm 0.03$) [139] rather than other alkyl chlorides, C_2H_5Cl ($m = -0.34 \pm 0.03$) [138] and $C_6H_{11}Cl$ ($m = -0.37 \pm 0.03$) [139], and in monochlorobenzene (C_6H_5Cl) [142] for $n_{Cl//}$ ($m = -0.21$) MO extending in-plane direction rather than $n_{Cl\perp}$ ($m = -0.30$) MO extending out-of-plane directions. Similar negative CEDPICS for $n_{Cl//}$ MOs of CH_2=CHCl ($m = -0.20$) [144], *o*-$C_6H_4Cl_2$ ($m = -0.19$) [147], *o*-$C_6H_4CH_3Cl$ ($m = -0.20$) [148] were observed. It was also found that the magnitude of attractive interaction around the Cl atom lone pair region perpendicular to the phenyl ring was *o*- > *p*- > *m*-$C_6H_4Cl_2$ [147].

Observed negative slope values of CEDPICS of C_6H_5Br for $n_{Br//}$ ($m = -0.41$) and $n_{Br\perp}$ ($m = -0.38$) MOs are larger than those of C_6H_5Cl [141]. Large negative CEDPICS for n_{Br} MOs were obtained for $C_{10}H_{15}Br$ ($m = -0.40$) and $C_6H_{11}Br$ ($m = -0.40, -0.41$) [140], while interaction potential calculations result in a comparable attractive well depth around the Br and Cl atoms. It should be noted that negative CEDPICS for ionization from n_I MOs for C_6H_5I ($m = -0.29, -0.33$) [142] and CH_2=CHI ($m = -0.22$,

−0.26) [144] were smaller than that for n_{Br} MOs, while large negative slope values of CEDPICS for $n_{I\perp}$ ($m = -0.41$) and $n_{I//}$ ($m = -0.35$) MOs were observed for alkyl iodide (CH_2ClI [119]).

Steric effects by intramolecular hydrogen bonding for 2-chloroethanol (ClC_2H_4OH) and 2-bromoethanol (BrC_2H_4OH) were investigated with CEDPICS [149]. In the most stable conformer, the magnitude of the hydrogen bonding in ClC_2H_4OH is stronger than BrC_2H_4OH, which results in large difference of negative slope values of CEDPICS for ionization from $n_{O(Cl)}$ ($m = -0.21$) and n_{Cl} MOs ($m = -0.43$, -0.41) rather than for $n_{O(Br)}$ ($m = -0.42$) and n_{Br} MOs ($m = -0.46$, -0.38).

6.3. *Ionic states of π electron molecules studied by 2D-PIES*

Ionic states of π electron molecules including electron correlation bands (satellite bands) originated from π-π^* shake-up process were studied by 2D-PIES. Negative CEDPICS for π ionization was observed for cyclic aromatic hydrocarbons in gas phase benzene (C_6H_6) [68, 106, 107, 150], naphthalene ($C_{10}H_8$), and anthracene ($C_{14}H_{10}$) [151] as well as solid phase chrysene ($C_{18}H_{12}$), perylene ($C_{20}H_{12}$), and coronene ($C_{24}H_{12}$) [152]. In the case of bonded 2 phenyl rings, large negative values CEDPICS about $m = -0.4$ or more were observed for π bands of biphenyl (C_6H_5–C_6H_5) [153] and [2,2]-paracyclophane ($C_{16}H_{16}$) [150], which can be explained by the attractive effect of another neighbouring phenyl ring. On the other hand, the neighbouring phenyl effect is limited in the case of diphenylacetylene (C_6H_5–C≡C–C_6H_5) [154], and small negative CEDPICS about $m = -0.2$ was observed for π bands. For σ ionization of diphenylacetylene, positive CEDPICS with a slope value of $m = +0.09$ was observed because of repulsive interactions around σ_{CH} bonds, and this positive value is similar to positive CEDPICS (around $m = +0.1$) for σ ionization of phenylacetylene (C_6H_5–C≡CH) [154] and benzene [107]. Large negative CEDPICS by attractive interactions around the rings was observed for ionization from cyclopentadienyl π orbitals of (η^5–C_5H_5)$_2$Co [155], while weak attractive or repulsive interactions were found around the cyclopentadienyl and cyclohexadienyl rings of (η^5–C_5H_5)Mn(CO)$_3$ and (η^6–C_6H_6)Cr(CO)$_3$ [122]. A satellite band was observed in PIES of benzene and toluene, though no corresponding band was found in photoelectron spectra [156]. This extra satellite band was assigned to a shake-up process because of theoretical calculations and the energy relation. Satellite bands observed as extra bands in 2D-PIES of benzene [68, 106, 150], biphenyl [153], diphenylacetylene [154], styrene [157], toluene [148], and (η^5–C_5H_5)$_2$Co [155] showed negative CEDPICS with similar slope values to π bands because of the π-π^* shake-up process associated with ionization from the π orbitals.

Intramolecular interorbital interactions between plural characteristic orbitals can determine the energy order of the MOs. The energy orders of frontier orbitals [158] have been studied with a concept of through-space/through-bond interactions between plural π or nonbonding orbitals [159]. In the case of 2,5-norbornadiene (C_7H_8) which has two symmetric π_{CC} groups in non-planar structure, through-space direct intramolecular interaction between overlapping two π_{CC} orbitals dominates the orbital energy order for symmetric orbital (ε^+) and antisymmetric orbital (ε^-) as $\varepsilon^+(\pi_{CC}) < \varepsilon^-(\pi_{CC})$, and ionization from the symmetric π_{CC} orbital showed the

larger band intensity and negative CEDPICS rather than the antisymmetric π_{CC} orbital because of the strong interaction in endo region [160]. On the other hand, 1,4-cyclohexadiene (C_6H_8) has two symmetric π_{CC} groups in a planar structure, and the orbital energy order is reversed ($\varepsilon^+(\pi_{CC}) > \varepsilon^-(\pi_{CC})$) to 2,5-norbornadiene, due to the intramolecular through-bond interaction with two methylene groups. Ionization from the symmetric π_{CC} MO showed smaller negative CEDPICS rather than the antisymmetric π_{CC} orbital, which was ascribed to the repulsive interaction around σ_{CH} bonds of the two methylene groups. Similarly, ionization from symmetric n_N orbital showed smaller negative CEDPICS rather than the antisymmetric n_N orbital for 1,4-diazabicyclo[2.2.2]octane (DABCO) because of the intramolecular through-bond interaction with ethylene groups and the repulsive interaction with He* around σ_{CH} bonds [160].

Relative band intensity and slope of CEDPICS for plural ionic states were compared to determine valence ionic states for overlapping bands corresponding to ionization from π orbitals and lone-pair electron orbitals on hetero atoms. Ionic states of five-membered hetero cyclic compounds were determined by 2D-PIES with negative CEDPICS between $m = -0.25$ and -0.40 for π ionization of pyrrole (C_4H_5N) [161], furan (C_4H_4O) [161], thiophene (C_4H_4S) [161], as well as 2- and 3-bromothiophene (C_4H_3SBr) [162]. In the case of thiazole (C_3H_3NS) [163], a strong attractive interaction was found for the nitrogen lone pair region for the in-plane direction, while a weak attractive interaction was found for the out-of-plane directions and the sulfur lone pair region in the in-plane direction. With the help of post Hartree–Fock *ab initio* MO calculations and large negative CEDPICS, observed satellite bands in 2D-PIES for pyrrole [161], thiophenes [161, 162], and thiazole [163] were assigned to ionization from π orbitals accompanied by a π-π^* or n-π^* shake-up process.

In the case of six-membered cyclic compounds including hetero atoms, 2D-PIES of azines (azabenzenes) [164] were observed. Obtained information on the anisotropic interaction around the molecule leads to reasonable assignments of the ionic states. Attractive interactions around the N atoms and repulsive interactions for the out-of-plane directions were found for *s*-triazine ($C_3H_3N_3$), which results in assignment of overlapping band 4 and 5 to $1a_2$ (π) and 5e′ orbitals by classical trajectory calculations on three-dimensional anisotropic potential surface [164], respectively (figure 16). Interactions for the out-of-plane directions were found to be attractive for pyridine (C_5H_5N), pyrazine, pyrimidine, and pyridazine ($C_4H_4N_2$). Ionization from nitrogen lone pair orbitals n_N results in large negative CEDPICS around $m = -0.35$ for *s*-triazine or $m = -0.5$ for azines except for *s*-triazine. When a vinyl group is introduced in order to prevent He* atoms from approaching to the nitrogen atom for 2-vinylpyridine [157], negative CEDPICS for ionization from n_N orbital became relatively small ($m = -0.33$) compared with 4-vinylpyridine (n_N, $m = -0.42$) [157]. Overlapping bands of *p*-benzoquinone ($C_6H_4O_2$) corresponding to four ionic states by *g* or *u* symmetric n_O or π_{CC} orbitals were examined with different slope of CEDPICS [165], and these bands were assigned in the ionization energy order of $n_O^- < n_O^+ < \pi_{CC}^- < \pi_{CC}^+$ with the help of analogous CEDPICS for the first four bands of tetramethyl-*p*-benzoquinone. An extra band was observed at $E_e \sim 7.2$ eV in He*(2^3S) PIES with negative CEDPICS of $m = -0.25$.

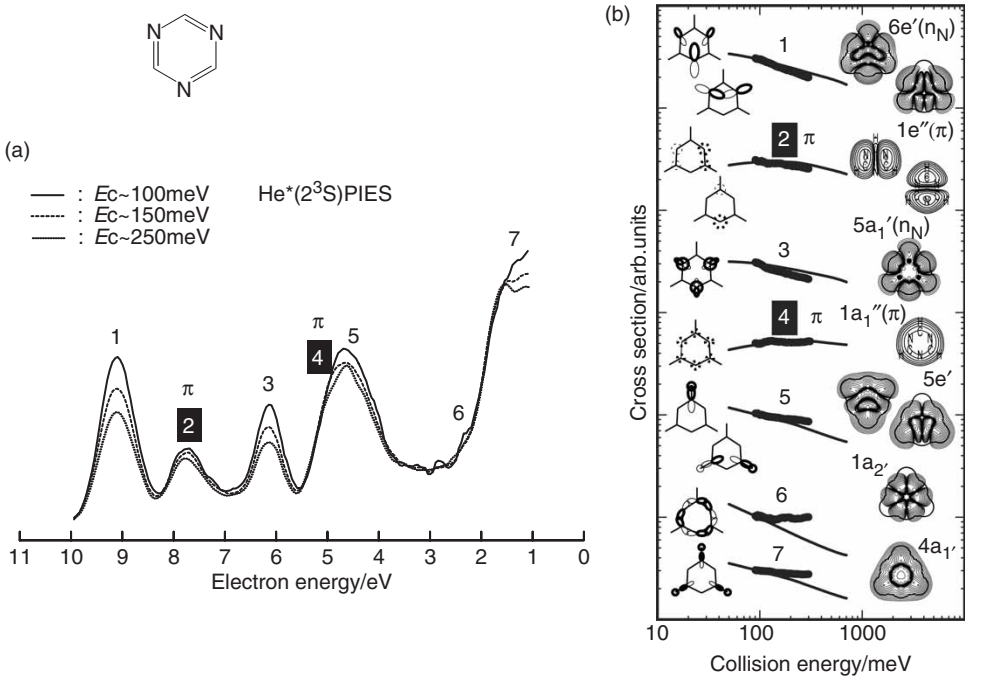

Figure 16. (a) CERPIES of *s*-triazine: solid curve at 86–108 meV; dotted curve at 136–166 meV; dashed curve at 220–284 meV. (b) CEDPICS for *s*-triazine. Thick lines show experimental data between 90 and 300 meV, and thin lines indicate theoretical data by trajectory calculations. Bands 2 and 4 show small negative CEDPICS, and they are assigned to ionization from π orbitals.

Assignments of valence ionic states of organic compounds including π electrons have been noted in theoretical studies by post Hartree–Fock methods because of large electron correlation effects. Consistency of assignments for ionic states with the results of 2D-PIES was examined by theoretical calculations for polycyclic [166–168] and five-membered heterocyclic [169] compounds.

6.4. *Autoionization process via superexcited states observed in 2D-PIES*

Observed Penning ionization electron spectra of $(CH_3)_4C$ and $(CH_3)_3CCl$ [55] showed unusual enhancement of C_{2s} bands, which was concluded to be due to the formation of an excimer-like state partly involving C_{2s} hole characters in the target molecules which induces intramolecular Auger-like autoionization transitions selectively from orbitals having C_{2s} characters. Vibrational structures of these C_{2s} bands were clearly different from those observed in UPS, and the slope of CEDPICS was slightly positive and rather flattened.

In addition to the main bands corresponding to valence ionic states or electron correlation (shake-up) bands of target molecules, some additional bands were observed in 2D-PIES for small molecules including chalcogens and halogens. Most of these bands were not obtained by post Hartree–Fock *ab initio* MO calculations for ionic

states of target molecules or out of Franck–Condon vibrational structure in PIES. The satellite bands can be assigned to autoionization via superexcited states [170] of molecules induced by a colliding He* atom ($M + A^* \rightarrow M^{**} + A \rightarrow M^+ + e^- + A$). Dissociation processes of some molecules were discussed on the basis of Penning electron–ion coincidence electron spectrum [171–173].

Different types of autoionization bands of chalcogen molecules were observed in 2D-PIES; one is autoionization bands (S) caused by excitation transfer resulting in large electron energy and large negative collision energy dependence for O_2 ($E_e \sim 7$–8 eV, $m = -0.40 \pm 0.12$) [36] as well as CS_2 ($E_e \sim 8$–9 eV, $m = -0.42$) [174], and another autoionization band (S*) is dissociative excitation transfer resulting in small electron energy and relatively small collision energy dependence for CS_2 ($E_e \sim 4.3$ eV, $m = -0.24$) as well as OCS ($E_e \sim 3$ eV, $m = 0.13$) [129]. The different CEDPICS of S* bands may be ascribed to the character of the interaction potential energy surface for collisional directions being favourable to the dissociation of M**. When a complex energy surface crossing in the entrance channel is connected to the ion-pair potential, negative band shifts and different slopes of CEDPICS compared to the S bands can be observed for O_2 ($E_e \sim 4$–5 eV, $m = -0.09 \pm 0.12$) as well as CS_2 ($E_e \sim 7.5$–8.5 eV, $m = -0.58$).

Similarly, two types of autoionization bands were observed for small halogenides. S bands at a large electron energy region showed large negative CEDPICS for HCl ($E_e \sim 6$ eV, $m = -0.38 \pm 0.03$) [175], CH_2ClI ($E_e \sim 7$–8 eV, $m = -0.37$) [119], and $CHBr_3$ ($E_e \sim 7$ eV, $m = -0.48$) [176]. These S bands can be assigned to autoionization into vibrationally excited states of the first ionic states. Autoionization bands S* by excitation transfer followed by molecular dissociation were observed at a small electron energy region with relatively smaller CEDPICS for HCl ($E_e \sim 0.5$–1.5 eV, $m = -0.15 \pm 0.01$) [175], CH_2ClI ($E_e \sim 1.0$–3.0 eV, $m = -0.26$) [119], CH_2BrCl ($E_e \sim 1.5$–2.0 eV, $m = -0.16$) [118], and $CHBrCl_2$ ($E_e \sim 1.5$ eV, $m = -0.19$) [118]. In figure 17(a), He I UPS and He*(2^3S) PIES of $CHBr_3$ are compared with EED spectra, and autoionization bands of S and S* were observed. The strong bands in the low electron energy region ($E_e < 5.5$ eV) can be explained by the good agreement with the estimated maximum electron energy released through autoionization to Br^+ ionic states in energy relation of the dissociation and autoionization process of $CHBr_3$ (figure 17b). The relative band intensity and the negative slope of CEDPICS for S* become larger as the number of Br increases for CH_3Br ($E_e \sim 1.0$ eV, $m = -0.10$), CH_2Br_2 ($E_e \sim 1.0$–2.5 eV, $m = -0.30$), and $CHBr_3$ ($E_e \sim 1.5$–2.5 eV, $m = -0.48$), which can be explained by spread of the attractive interaction region around the Br atoms [176]. When Ne*($^3P_{0,2}$) PIES bands of $CHBr_3$ was compared with He*(2^3S) PIES bands taking the smaller excitation energy of Ne* than He*(2^3S) by ca. 3 eV into account, the band intensity enhancement was found in $E_e \sim 1.0$–2.5 eV region of Ne*($^3P_{0,2}$) PIES. This band enhancement in Ne*($^3P_{0,2}$) PIES was explained by autoionization of superexcited Rydberg Br atoms generated by collision with Ne*($^3P_{0,2}$) [176].

An autoionization process via superexcited states was observed as additional bands with extra kinetic energies of 1–2 eV in comparison with those expected for vertical ionization in PIES of van der Waals clusters of rare gas atoms [64, 177] and molecules [178]. 2D-PIES measurements of molecular clusters should be interesting topics when the velocity-resolved measurement can be reliably applied to such extremely low density targets.

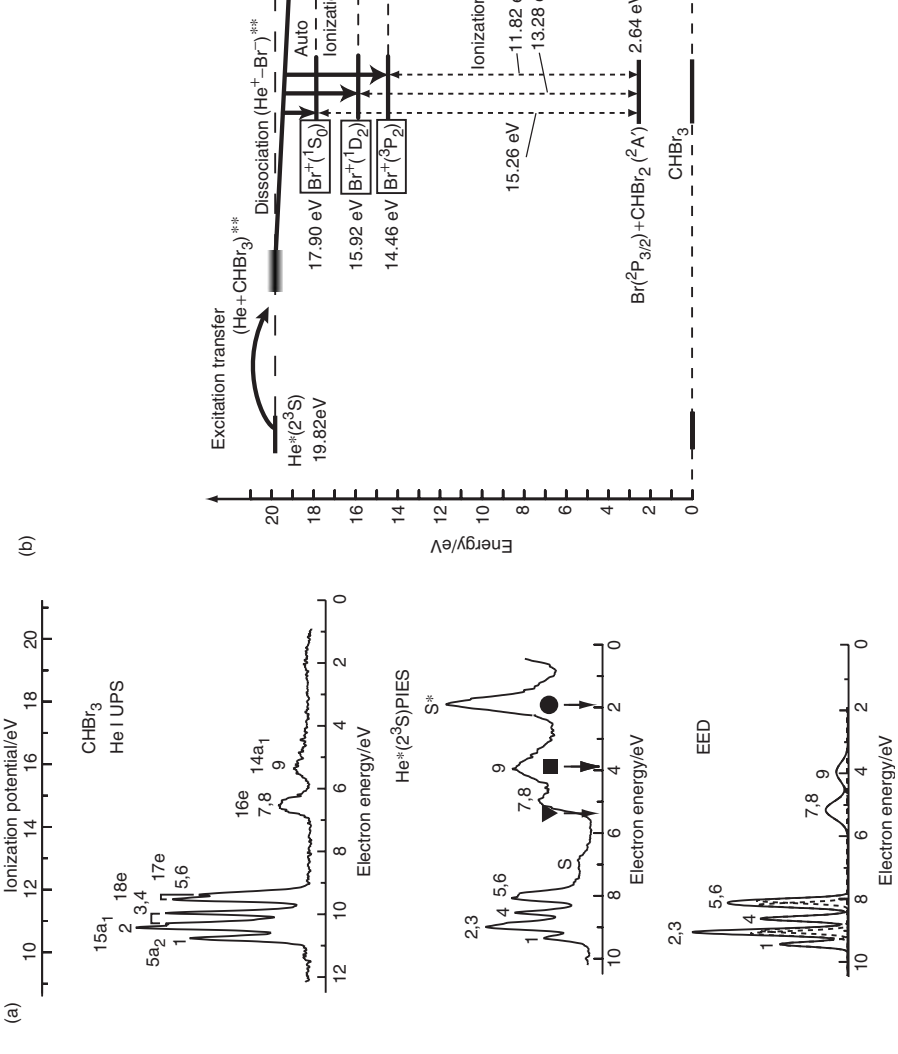

Figure 17. (a) He I UPS and He*(2^3S) PIES of $CHBr_3$ compared with an EED spectrum, and (b) the energy analysis of the dissociation and autoionization process of $CHBr_3$ accounting for S* band in He*(2^3S) PIES. Filled symbols (▼■●) indicate estimated maximum electron energies released through autoionization to Br^+ ionic states.

7. Experimental determination of Dyson orbital and electron ejection functions

The concept of molecular orbitals plays an important role in chemistry, and experimental observation of the MO pattern was suggested by Fukui [179] on the basis of successful studies on chemical reactions by the MO theory [180, 181]. However, it is well-known that MO functions have been used as good tool in *ab initio* MO calculations, and a direct measurement of MOs will be quite difficult. In ionization events, one electron orbital which is known as Dyson orbital can be directly connected to MOs, and the shape of Dyson orbitals can be determined as electron density functions through ionization experiments. Different from other experimental methods using photons or electrons, ionization of molecules by collision with a metastable atom is excellent in probing outer properties of molecules, which are of great importance in many aspects of chemical and physical phenomena that occur when a molecule contacts with other species. The shape of the Dyson orbital can be considerably different from an SCF (self-consistent field) MO due to the electron correlation and the orbital relaxation effects. Although 2D-PIES data can be connected to radial dependence of ionization width $\Gamma(R)$ or the electron distribution of the MO to be ionized and the interaction potential V^*, calculated partial ionization cross-sections sensitively depend on the shape of the orbital functions. When wave functions of a target molecule M for the neutral ground state of an N-electron system (Ψ_0^{N}) and the respective cationic state of an $(N-1)$-electron system ($\Psi_j^{\mathrm{N-1}}$) are introduced, the ionization width in equation (22) can be shown as

$$\Gamma^{(i)} = 2\pi\rho^{(j)}\left|\left\langle\Phi_0|H_{\mathrm{el}}|\Phi^{(j)}\right\rangle\right|^2 = 2\pi\rho^{(j)}\left|\left\langle\Psi_0^{\mathrm{N}}\psi_{\mathrm{He}*}|H_{\mathrm{el}}|\Psi_j^{\mathrm{N-1}}\psi_{\mathrm{He}}\phi_\varepsilon\right\rangle\right|^2. \tag{30}$$

The two-electron exchange integral can be converted into the product of overlap integrals, and the following equation can be obtained,

$$\left\langle\Phi_0|H_{\mathrm{el}}|\Phi^{(j)}\right\rangle \approx \left\langle\Psi_0^{\mathrm{N}}|\Psi_j^{\mathrm{N-1}}\psi_{1s}\right\rangle\left\langle\psi_{2s}|\phi_\varepsilon\right\rangle. \tag{31}$$

The Dyson orbital for the j-th cationic state of M can be defined as an overlap of wave functions for a neutral ground state and an ionic state, $\langle\Psi_0^{\mathrm{N}}|\Psi_j^{\mathrm{N-1}}\rangle$, based on the generalized overlap amplitude. It follows that the Dyson orbital (ϕ_j^{Dyson}) can be a one-electron orbital function with taking electron correlation and orbital relaxation effects into consideration. Then equations (31) and (25) can be expressed as follows,

$$\left\langle\Phi_0|H_{\mathrm{el}}|\Phi^{(j)}\right\rangle \approx \left\langle\phi_j^{\mathrm{Dyson}}|\psi_{1s}\right\rangle\left\langle\psi_{2s}|\phi_\varepsilon\right\rangle, \tag{32}$$

$$\Gamma^{(j)} \approx K^{(j)}\left|\left\langle\phi_j^{\mathrm{Dyson}}|\psi_{1s}\right\rangle\right|^2, \tag{33}$$

Here, it should be noted that the Dyson orbital can be observable upon the ionization event, and metastable atoms can sensitively probe spatial distribution of Dyson orbitals

in the exterior region with collision-energy-resolved measurements which can lead to spatially limited (or selected) probing around the molecular surface as shown in figure 10. When anisotropic functions of both V^* and Γ are consistently calculated, Dyson orbitals can be determined by comparing experimental 2D-PIES data with theoretical ones [93, 182].

Since the angular distribution of Penning electrons has strong relation with the interaction potential [13, 183, 184], the ionic state [55, 68, 185], as well as the electron ejection functions [13, 183], angular-/collision-energy-/electron-energy-resolved three-dimensional Penning ionization electron spectroscopy (3D-PIES) can offer important data to determine the electron ejection functions with classical trajectory calculations based on already calculated V^* and Γ [94].

7.1. *Dyson orbital for ionization of N_2 by He**

In earlier studies, exterior electron distributions corresponding to ionic states in PIES were found to depend crucially on the qualities of wave function tails for various SCF MOs [186, 187]. The radial dependence of the exterior electron density for SCF MOs outside the molecular surface with the largest basis set showed [186] a consistent asymptotic decay with the simple exponential form with the decay parameter determined from the lowest ionization energy [45–48].

Figure 18(a) shows observed and calculated CEDPICS with SCF MOs by a minimal basis set (SCF/Min) and the Li-model interaction potential (broken lines) as well as the best optimized MOs (CEDPICS MOs) and the interaction potential (solid lines).

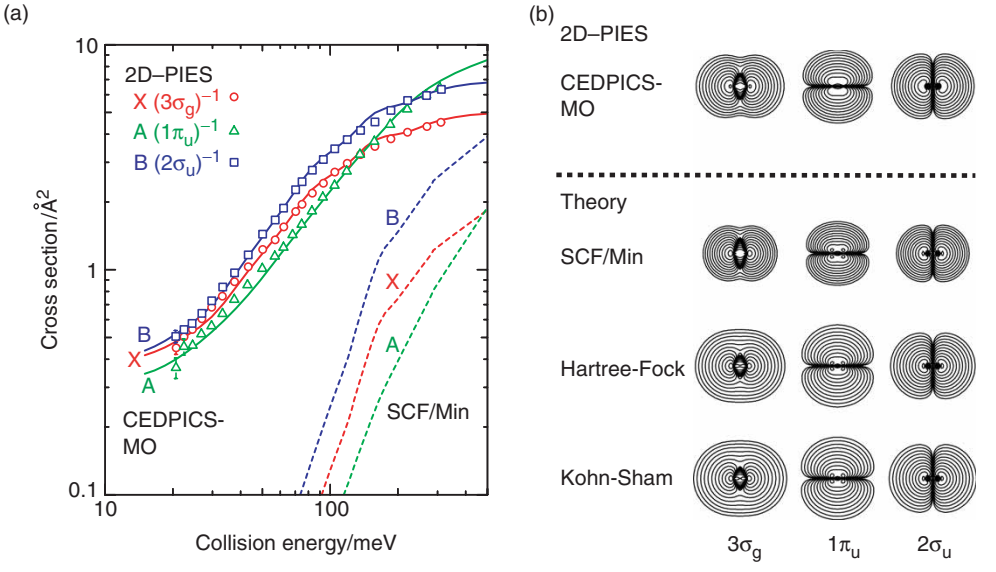

Figure 18. [Colour online] (a) CEDPICS of N_2/He*(2^3S) by SCF MOs with minimal basis set (SCF/Min) and best optimized MOs (CEDPICS-MO), and (b) electron density contour maps corresponding to three ionic states of N_2 for various MOs by experiment (CEDPICS-MO) and theory (SCF/Min, Hartree–Fock, and Kohn–Sham).

The optimized results gave excellent agreement with experimental CEDPICS in the observed collision energy range. Electron density contour maps for various MOs corresponding to the observed three ionic states of N_2 are shown in figure 18(b). The CEDPICS MOs are compared with the SCF/Min, and 138-contracted Gaussian type functions for the near Hartree–Fock limit (HF) as well as a Kohn–Sham DFT (density functional theory) calculation (KS) [188, 189] with the well-known hybrid correlation functional, B3LYP [190]. The large basis set of 138-CGTF (contracted Gaussian-type functions) consists of [7s6p] CGTF of the cc-pV6Z basis and [4d2f] CGTF used in the study of Feller *et al.* [191]. The small spreading of SCF/Min results in rapid positive CEDPICS due to the large magnitude of the overlap integral for the transition rate at the shorter distances between N_2 and He*. In order to compare the CEDPICS MOs with SCF MOs, electron densities $\rho_e^{(j)}$ are plotted as a function of distance R from the centre of N_2 in figure 19(a). The SCF/Min electron density rapidly decreases as the increase of the distance, while HF and KS SCF orbitals are extending outside and comparable with the CEDPICS MOs. From the slope of the log $\rho_e^{(j)}$ vs. R plot, the CEDPICS MOs show more compact electron distributions than HF and KS SCF orbitals.

In order to obtain theoretical Dyson orbitals, a post Hartree–Fock calculations by the symmetry adapted cluster expansion and configuration interaction method (SAC/SAC-CI) [192, 193] for the overlap $\langle \Psi_0^N | \Psi_i^{N-1} \rangle$ was performed. The basis set of cc-pV5Z was adopted because of lower total energy than the case of [7s6p4d2f] CGTF. As shown in figure 19(a), the theoretical Dyson orbital was found to be spatially compact rather than HF SCF orbitals, which agrees well the experimentally determined CEDPICS MOs.

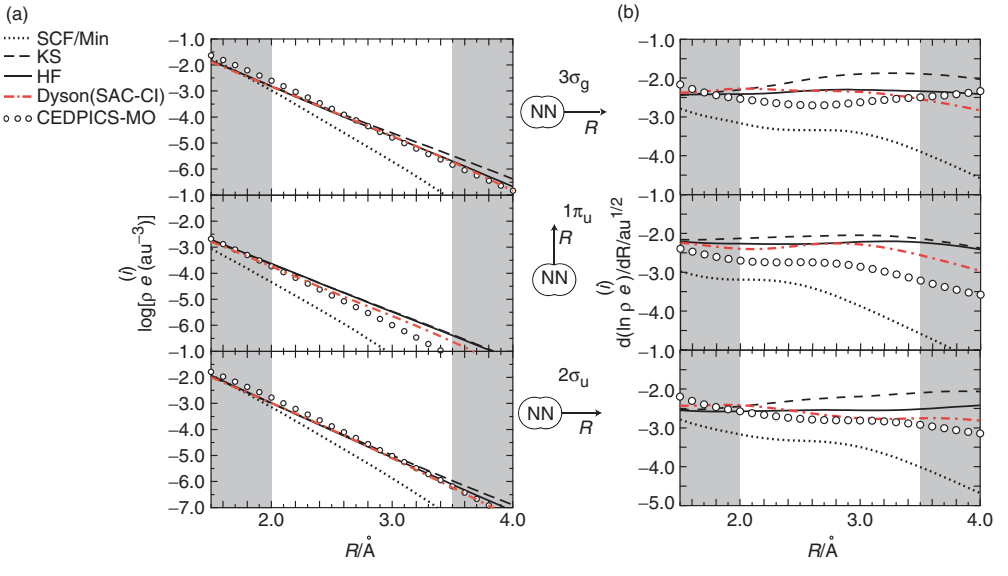

Figure 19. [Colour online] (a) Electron density (ρ) of various MOs as a function of distance R from the centre of N_2 in log $\rho_e^{(i)}$ vs. R plot, and (b) logarithmic derivative of electron densities ($d(\ln \rho_e^{(i)})/dR$) for various MOs as well as Dyson orbitals obtained by SAC-CI calculations.

The electron density of a Hartree–Fock orbital is known [45–48] to decay exponentially at long distance with a parameter α determined by the energy of HOMO ($\varepsilon_{\mathrm{HOMO}}$) as

$$\rho_e^{(j)}(R) = |\phi_j(R)|^2 \sim \exp(-2\alpha R),\ \alpha = (-2\varepsilon_{\mathrm{HOMO}})^{1/2}. \tag{34}$$

The decay parameters of electron densities for various MOs can be examined from a logarithmic derivative of the electron density by $d(\ln \rho_e^{(j)})/dR \sim (-2\alpha)$. The logarithmic derivatives of SCF MOs, CEDPICS MOs, and theoretical Dyson orbitals corresponding to three ionic states are shown in figure 19(b). The obtained logarithmic derivatives of HF SCF MOs are near to the ideal asymptotic value ($-2\alpha = -2.22\,\mathrm{a.u.}^{1/2}$) determined by the energy of HOMO of N_2 ($\varepsilon_{\mathrm{HOMO}} = -0.61415\,\mathrm{a.u.}$). On the other hand, SCF/Min and KS SCF MOs deviate from the constant conversion value of $-2.22\,\mathrm{a.u.}^{1/2}$. It should be noted that logarithmic derivatives KS SCF orbitals with different hybrid correlation functionals are larger than the value of $-2.22\,\mathrm{a.u.}^{1/2}$, which can be connected to the large extending of KS SCF MOs. The logarithmic derivatives of CEDPICS MOs and theoretical Dyson orbitals are similar to or smaller than those of HF SCF MOs in the middle range of R (2.0–3.5 Å). Since the asymptotic decay of Dyson orbitals may be related to their eigenvalues by $\alpha = (2I_j)^{1/2}$ with respective ionization energy I_j, a characteristic behaviour of Dyson orbital can be obtained for each ionic state. The similar R dependence of the logarithmic derivatives between CEDPICS MOs and theoretical Dyson orbitals indicates the high sensitivity of CEDPICS in order to determine the outer shape of Dyson orbitals experimentally.

7.2. *Electron ejection functions for collisional ionization of N_2 by He**

Ebding and Niehaus have measured the angular distributions of electrons emitted in Penning ionization for He*(2^3S) with Ar, Kr, Xe, CO, N_2, and Hg [181] as a function of the angle θ with respect to the initial He*(2^3S) beam vector. The angular distributions were found to be strongly anisotropic and asymmetric in the case of practically no or very small interaction potential well. Niehaus measured the variation of the angular distribution for Ar–He*(2^3S) system with changing collision energy from 80 meV to 350 meV as dividing the thermal distribution into some parts for a similar intensity using the time-of-flight (TOF) technique [13]. They found that the behaviour of the angular distribution curves was insensitive to collision energies in the range 80–350 meV, probably because of a weak attractive interaction between Ar and He*(2^3S). Mitsuke *et al*. changed the collision energy with controlling nozzle temperature and measured the angular distribution of electrons for He*(2^3S)–H_2S [182]. They found that the angular distribution curves varied with the collision energy in this system, because of the deflection of trajectories by a long-range attractive potential for He*(2^3S)–H_2S. State-resolved angular distributions of Penning electrons were connected to interaction potential or mechanism of ionization [55, 68, 185]. The laboratory angular distributions of ejected electrons in Penning ionization for three ionic states of N_2–He*(2^3S) at three collision energies are shown in figure 20(a) [94]. Symbols and curves are experimental and calculated data, respectively. All ionic states show asymmetric angular distribution

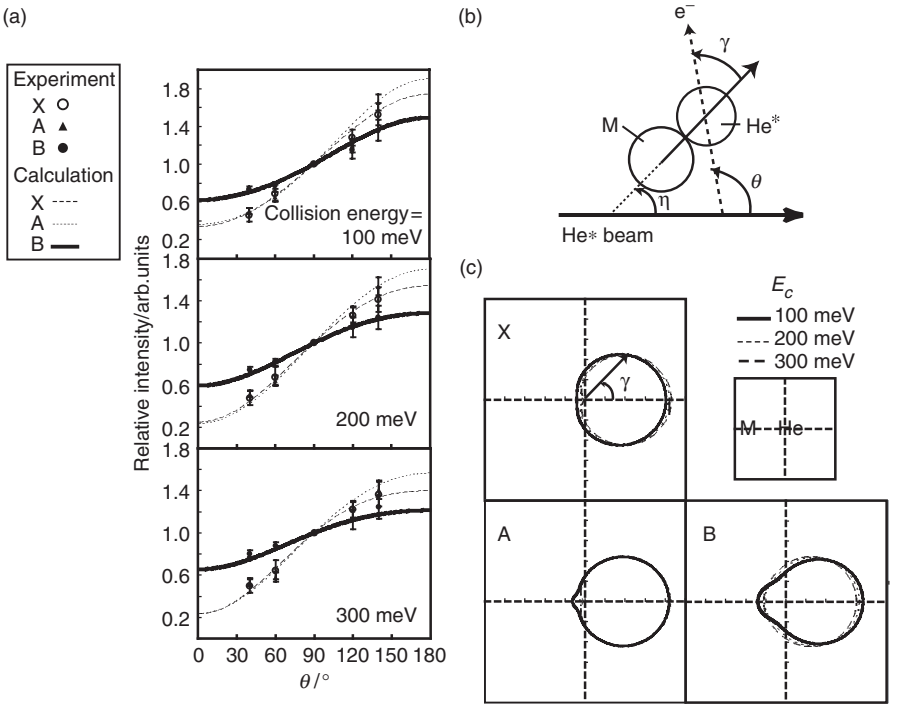

Figure 20. (a) Angular distribution of Penning electrons by angle resolved measurement (symbols) as well as trajectory calculation (lines) for N_2/He*(2^3S) at collision energy $E_c = 100$, 200, and 300 meV. (b) Electron emission direction θ ($=\eta+\gamma$) with angles η between M–He* vector and He* beam, and γ between M–He* vector and electron emission direction. (c) Internal angular (γ) distributions corresponding to three ionic states for electron emission originated from a helium atom at collision energy $E_c = 100$, 200, and 300 meV.

with respect to $\theta = 90^\circ$, which indicates that the ejection direction of electrons strongly depends on the orientation of the target molecule and He*(2^3S) during ionization. The angular distribution of $B^2\sum_u^+$ state shows smaller anisotropy than $X^2\sum_g^+$ and $A^2\Pi_u$ states. With the increase of collision energy, anisotropy of the angular distribution is decreased in all ionic states beyond $\theta = 90^\circ$, which can be explained by the increase of grazing (or non-colliding) trajectories with a high reaction probability near the surface of the closest approach as shown in the reaction probability maps.

We obtained information on internal angular distribution for electron emission originated from a helium atom (figure 20b) for N_2–He*(2^3S) [94] from trajectory calculations as Niehaus showed for Ar–He*(2^3S) [13]. The internal angular distributions can be related to the wave functions of ejected electrons. The internal angular distribution of $A^2\Pi_u$ state inclines to helium and is similar to that of $X^2\sum_g^+$ state regardless of different orbital symmetry, which is consistent with the electron exchange mechanism in which 2s electrons are ejected. The shape of asymmetric angular distribution may be due to the polarization effect by hybridization with a 2p orbital in interaction with N_2.

8. Concluding remarks

In order to elucidate chemi-ionization stereodynamics between metastable atoms and target molecules without any control of orientation or alignment of molecules, we have developed new methods and techniques in step-by-step way as summarized in this article for (a) experiment improvements such as an intense metastable He* beam, the velocity selected measurement, the efficient electron collection by magnetic fields, and the automated accumulation of electron signals as functions of collisional and electron kinetic energies, as well as (b) theoretical treatments such as the interaction potential energy calculations for entrance and exit channels, the classical trajectory method with the ionization width for individual ionic state, and the electron ejection functions. Since Penning ionization has spatial limitation in the transition probability in the outer region of target molecules due to the interaction potential wall, a collision-energy-resolved measurement of the metastable atomic beam enables us to study characteristics of both the molecular orbital and the anisotropic molecular surface in the outer region when it is combined with an ionic-state-selected measurement by electron spectroscopy. The interaction potential energy surface between He* and the target molecules has strong anisotropy, and the anisotropic interactions result in individual slope of CEDPICS (collision energy dependence of partial ionization cross-sections) in the observed collision energy range. The different slope of CEDPICS enables us to determine assignments of ionic states and satellite bands for many molecules. Utilizing observed CEDPICS and CERPIES (collision-energy-resolved PIES) obtained from continuous 2D-PIES data, classical trajectory calculations can extract information on interaction potential energy surfaces as well as dynamical aspects of collisional ionization processes such as opacity functions for individual ionic states, angular distributions of ejected electrons, and radial characteristics of Dyson orbitals which can be compared with *ab initio* SCF molecular orbitals.

He* PIES has been applied to liquid [194] and solid [195] surfaces in order to study the composition, orientation, or distribution of MOs at the outermost surface layer. In the future prospect, making good use of its usefulness to study reaction dynamics and electronic states, 2D-PIES may be applied to liquid or solid surfaces in order to investigate intermolecular interaction of heterogeneous adsorbate on metal surfaces or solutes on solvents by means of collision-energy-resolved He* metastable atoms. In this relation, different slopes of CEDPICS have been obtained for solid phase aromatic hydrocarbons deposited on a metal surface [152].

Quantitative analyses of anisotropic interaction potentials, ionic states, stereodynamics of collisional ionization, and orbital functions for larger systems will be possible with the development of computational ability as well as sophisticated experiments.

Acknowledgements

The authors wish to thank all those people who gave important contributions to the topics in this article, especially to Prof. K. Mitsuke, Dr. T. Takami, Prof. H. Yamakado, Dr. T. Ogawa, Mr. T. Yamata, Prof. T. Pasinszki, Prof. F. Misaizu, Dr. Y. Yamakita,

Dr. K. Imura, Dr. S. X. Tian, Dr. M. Yamazaki, Dr. T. Horio, and Mr. S. Maeda. The authors have been financially supported by the Grants-in-Aid from Ministry of Education, Culture, Sports, Science and Technology (MEXT) as well as Japan Society for the Promotion of Science (JSPS).

References

[1] For example, R. D. Levine, and R. B. Bernstein, *Molecular Reaction Dynamics and Chemical Reactivity* (Oxford University Press: New York, 1987).
[2] S. Hoshino and K. Ohno, J. Am. Chem. Soc. **119,** 8276 (1997).
[3] D. W. Turner, C. Baker, A. D. Baker, and C. R. Brundle, *Molecular Photoelectron Spectroscopy* (Wiley, New York, 1970).
[4] K. Siegbahn, C. Nordling, G. Johansson, J. Hedman, P. F. Heden, K. Hamrin, U. Gelius, T. Bergmark, L. O. Werme, R. Manne, and Y. Baer, *ESCA Applied to Free Molecules* (North-Holland, Amsterdam, 1969).
[5] C. R. Brundle and A.D. Baker, *Electron Spectroscopy – Theory, Techniques, and Applications* (Academic Press, New York, 1977) Vol. 1, .
[6] J. W. Rabalais, *Principles of Ultraviolet Photoelectron Spectroscopy* (Wiley, New York, 1977).
[7] K. Kimura, S. Katsumata, Y. Achiba, T. Yamazaki, and S. Iwata, *Handbook of He I Photoelectron Spectra of Fundamental Organic Molecules* (Japan Scientific Societies Press, Tokyo, 1981).
[8] U. Amaldi, A. Egidi, R. Marconero, and G. Pizzella, Rev. Sci. Instrum. **40,** 1001 (1969).
[9] E. Weigold and I. E. McCarthy, *Electron Momentum Spectroscopy* (Kluwer Academic/Plenum, New York, 1999), and references cited therein.
[10] Y. Zheng, J. J. Neville, and C. E. Brion, Science **270,** 786 (1995).
[11] F. M. Penning, Naturwissenschaften **15,** 818 (1927).
[12] A. J. Yencha, in *Electron Spectroscopy – Theory, Techniques, and Applications*, edited by C. R. Brundle and A. D. Baker (Academic Press, New York, 1984) Vol. 5, .
[13] A. Niehaus, Adv. Chem. Phys. **45,** 399, and references cited therein (1981).
[14] P. E. Siska, Rev. Mod. Phys. **65,** 337, and references cited therein (1993).
[15] R. E. Olson, Phys. Rev. A **6,** 1025 (1972).
[16] H. Nakamura, J. Phys. Soc. Jpn. **26,** 1473 (1969).
[17] W. H. Miller, Chem. Phys. Lett. **4,** 627 (1970).
[18] W. H. Miller, J. Chem. Phys. **52,** 3563 (1970).
[19] E. Illenberger and A. Niehaus, Z. Phys. B **20,** 3590 (1975).
[20] V. Čermák, J. Chem. Phys. **44,** 3781 (1966).
[21] H. Hotop and A. Niehaus, Int. J. Mass Spectrom. Ion Phys. **5,** 415 (1970).
[22] D. S. C. Yee, W. B. Stewart, C. A. McDowell, and C. E. Brion, J. Electron Spectrosc. Relat. Phenom. **7,** 377 (1975).
[23] V. Čermák and A. J. Yencha, J. Electron Spectrosc. Relat. Phenom. **8,** 109 (1976).
[24] T. Munakata, K. Kuchitsu, and Y. Harada, J. Electron Spectrosc. Relat. Phenom. **20,** 235 (1980).
[25] T. Munakata, K. Ohno, and Y. Harada, J. Chem. Phys. **72,** 409 (1980).
[26] K. Ohno, H. Mutoh, and Y. Harada, J. Am. Chem. Soc. **105,** 4555 (1983).
[27] K. Ohno and Y. Harada, in *Theoretical Models of Chemical Bonding*, edited by Z. B. Maksić (Springer, Berlin, 1991), Part 3, p. 199.
[28] K. Ohno, S. Matsumoto, and Y. Harada, J. Chem. Phys. **81,** 2183 (1984).
[29] K. Ohno, S. Matsumoto, and Y. Harada, J. Chem. Phys. **81,** 4447 (1984).
[30] H. Hotop, E. Kolb, and J. Lorenzen, J. Electron Spectrosc. Relat. Phenom. **16,** 213 (1979).
[31] H. Hotop, in *Electronic and Atomic Collisions*, edited by N. Oda and K. Takayanagi (North-Holland, Amsterdam, 1979).
[32] E. J. Longley, D. C. Dunlavy, M. F. Falcetta, H. M. Bevsek, and P. E. Siska, J. Phys. Chem. **97,** 2097 (1993).
[33] D. C. Dunlavy, D. W. Martin, and P. E. Siska, J. Chem. Phys. **93,** 5347 (1990).
[34] D. C. Dunlavy and P. E. Siska, J. Phys. Chem. **100,** 21 (1996).
[35] F. Biondini, B. Brunetti, P. Candori, F. De Angelis, S. Falcinelli, F. Tarantelli, M. Moix Teixidor, F. Pirani, and F. Vecchiocattivi, J. Chem. Phys. **122,** 164307 (2005).
[36] K. Mitsuke, T. Takami, and K. Ohno, J. Chem. Phys. **91,** 1618 (1989).
[37] K. Ohno, T. Takami, K. Mitsuke, and T. Ishida, J. Chem. Phys. **94,** 2675 (1991).
[38] K. Ohno, H. Yamakado, T. Ogawa, and T. Yamata, J. Chem. Phys. **105,** 7536 (1996).
[39] N. Kishimoto, J. Aizawa, H. Yamakado, and K. Ohno, J. Phys. Chem. A **101,** 5038 (1997).

[40] K. Ohno, Bull. Chem. Soc. Jpn. **77,** 887 (2004).
[41] K. Ohno, M. Yamazaki, S. Maeda, and N. Kishimoto, J. Electron Spectrosc. Relat. Phenom. **142,** 283 (2005).
[42] J. H. D. Eland, *Photoelectron Spectroscopy* (Butterworth, London, 1974).
[43] H. Hotop and A. Niehaus, Z. Phys. **228,** 68 (1969).
[44] H. Hotop and A. Niehaus, Chem. Phys. Lett. **8,** 497 (1971).
[45] N. C. Handy, M. T. Marron, and H. J. Silverstone, Phys. Rev. **180,** 45 (1969).
[46] M. M. Morrell, R. G. Parr, and M. Levy, J. Chem. Phys. **62,** 549 (1975).
[47] J. Katriel and E. R. Davidson, Proc. Natl. Acad. Sci. USA **77,** 4403 (1980).
[48] T. Ishida and K. Ohno, Theor. Chim. Acta **81,** 355 (1992).
[49] K. Ohno, S. Hoshino, H. Yamakado, N. Kishimoto, T. Takami, and T. Ogawa, unpublished work.
[50] H. Hotop, Radiat. Res. **59,** 379, and references cited therein (1974).
[51] H. Haberland, Y. T. Lee, and P. E. Siska, Adv. Chem. Phys. **45,** 487, and references cited therein (1981).
[52] H. Hotop, T. E. Roth, M.-W. Ruf, and A. J. Yencha, Theor. Chem. Acc. **100,** 36 (1998).
[53] S. F. Boys and F. Bernardi, Mol. Phys. **19,** 553 (1970).
[54] T. Horio, T. Hatamoto, S. Maeda, N. Kishimoto, and K. Ohno, J. Chem. Phys. **124,** 104308 (2006).
[55] T. Takami, K. Mitsuke, and K. Ohno, J. Chem. Phys. **95,** 918 (1991).
[56] B. Brutschy and H. Haberland, J. Phys. E **10,** 90 (1977).
[57] D. W. Fahey, W. F. Parks, and L. D. Schearer, J. Phys. E **13,** 381 (1980).
[58] E. S. Fry and W. L. Williams, Rev. Sci. Instrum. **40**, 1141 (1969).
[59] H. Hotop, A. Niehaus, and A. L. Schmeltekopf, Z. Phys. **229**, 1 (1969).
[60] T. Horio, T. Hatamoto, N. Kishimoto, and K. Ohno, Chem. Phys. Lett. **397,** 242 (2004).
[61] A. Robert, O. Sirjean, A. Browaeys, J. Poupard, S. Nowak, *et al*., Science **292,** 461 (2001).
[62] N. Herschbach, P. J. J. Tol, W. Vassen, W. Hogervorst, G. Woestenenk, *et al*., Phys. Rev. Lett. **84,** 1874 (2000).
[63] G. R. Woestenenk, J. W. Thomsen, M. van Rijnbach, P. Van der Straten, and A. Niehaus, Rev. Sci. Instrum. **72,** 3842 (2001).
[64] K. Ohno, H. Tanaka, Y. Yamakita, R. Maruyama, T. Horio, and F. Misaizu, J. Electron Spectrosc. Relat. Phenom. **112,** 115 (2000).
[65] D. J. Auerbach, in *Atomic and Molecular Beam Methods*, edited by G. Scoles (Oxford University Press, New York, 1988) Vol. 1, p. 362.
[66] For example, G. Comsa, R. David, and B. J. Schumacher, Rev. Sci. Instrum. **52,** 789 (1981).
[67] H. G. Hecht, *Mathematics in Chemistry. An Introduction to Modern Methods* (Prentice Hall, London, 1990).
[68] T. Takami and K. Ohno, J. Chem. Phys. **96,** 6523 (1992).
[69] T. Hsu and J. L. Hirshfield, Rev. Sci. Instrum. **47,** 236 (1976).
[70] G. Beamson, H. Q. Porter, and D. W. Turner, Nature (London) **290,** 555 (1981).
[71] Y. Yamakita, H. Tanaka, R. Maruyama, F. Misaizu, and K. Ohno, Rev. Sci. Instrum. **71,** 3042 (2000).
[72] J. L. Gardner and J. A. R. Samson, J. Electron Spectrosc. Relat. Phnom. **8,** 469 (1976).
[73] T. Ishida and K. Horime, J. Chem. Phys. **105,** 5380 (1996).
[74] T. Ishida, J. Chem. Phys. **105,** 1392 (1996).
[75] M. Alberti, J. M. Lucas, B. Brunetti, F. Pirani, M. Stramaccia, M. Rosi, and F. Vecchiocattivi, J. Phys. Chem. A **104,** 1405 (2000).
[76] B. Haug, H. Morgner, and V. Staemmler, J. Phys. B **18,** 259 (1985).
[77] F. Biondini, B. Brunetti, P. Candori, F. DeAngelis, S. Falcinetti, F. Pirani, F. Tarantelli, and F. Vecchiocattivi, J. Chem. Phys. **122,** 164308 (2005).
[78] T. Ogawa and K. Ohno, J. Chem. Phys. **110,** 3773 (1999).
[79] T. Ogawa and K. Ohno, J. Phys. Chem. A **103,** 9925 (1999).
[80] M. Yamazaki, N. Kishimoto, M. Kurita, T. Ogawa, K. Ohno, and K. Takeshita, J. Electron Spectrosc. Relat. Phenom. **114–116,** 175 (2001).
[81] M. Yamazaki, S. Maeda, N. Kishimoto, and K. Ohno, Chem. Phys. Lett. **355,** 311 (2002).
[82] M. Yamazaki, S. Maeda, N. Kishimoto, and K. Ohno, J. Chem. Phys. **117,** 5707 (2002).
[83] S. Maeda, M. Yamazaki, N. Kishimoto, and K. Ohno, J. Chem. Phys. **120,** 781 (2004).
[84] L. S. Cederbaum, J. Phys. B **8,** 290 (1975).
[85] J. V. Ortiz, J. Chem. Phys. **89,** 6348 (1988).
[86] T. Koopmans, Physica **1,** 104 (1933).
[87] T. Ishida and H. Katagiri, J. Phys. Chem. A **105,** 9379 (2001).
[88] T. Ishida, Chem. Phys. Lett. **191,** 1 (1992).
[89] W. H. Miller and H. Morgner, J. Chem. Phys. **67,** 4923 (1977).
[90] R. S. Mulliken, J. Chim. Phys. **46,** 497 (1949).
[91] V. N. Demikov, Soviet Phys. JETP **18,** 138 (1964).
[92] S.-I. Choi, J. Jortner, S. A. Rice, and R. Silbey, J. Chem. Phys. **41,** 3294 (1964).

[93] M. Yamazaki, S. Maeda, and K. Ohno, Chem. Phys. Lett. **391,** 366 (2004).
[94] Y. Hanzawa, N. Kishimoto, M. Yamazaki, and K. Ohno, Chem. Phys. Lett. **426,** 43 (2006).
[95] E. Illenberger and A. Niehaus, Z. Phys. B **20,** 33 (1975).
[96] A. Pesnelle, G. Watel, and C. Manus, J. Chem. Phys. **62,** 3590 (1975).
[97] M. R. Woodard, R. C. Sharp, M. Seely, and E. E. Muschlitz Jr, J. Chem. Phys. **69,** 2978 (1978).
[98] T. P. Parr, D. M. Parr, and R. M. Martin, J. Chem. Phys. **76,** 316 (1982).
[99] L. Appolloni, B. Brunetti, J. Hermanussen, F. Vecchiocattivi, and G. G. Volpi, J. Chem. Phys. **87,** 3804 (1987).
[100] N. Kishimoto, M. Furuhashi, and K. Ohno, J. Electron Spectrosc. Related. Phenom. **88–91,** 143 (1998).
[101] K. Ohno, M. Yamazaki, N. Kishimoto, T. Ogawa, and K. Takeshita, Chem. Phys. Lett. **332,** 167 (2000).
[102] T. H. Lee and J. W. Rabalais, J. Chem. Phys. **61,** 2747 (1974).
[103] W. H. Miller, C. A. Slocomb, and H. F. Schaefer III, J. Chem. Phys. **56,** 1347 (1972).
[104] T. Horio, M. Yamazaki, S. Maeda, T. Hatamoto, N. Kishimoto, and K. Ohno, J. Chem. Phys. **123,** 194308 (2005).
[105] T. Horio, S. Maeda, N. Kishimoto, and K. Ohno, J. Phys. Chem. A **110,** 11010 (2006).
[106] M. Yamazaki, S. Maeda, N. Kishimoto, and K. Ohno, J. Chem. Phys. **122,** 044303 (2005).
[107] T. Horio, R. Maruyama, N. Kishimoto, and K. Ohno, Chem. Phys. Lett. **384,** 73 (2004).
[108] M. P. Sinha, C. D. Caldwell, and R. N. Zare, J. Chem. Phys. **61,** 491 (1974).
[109] D. P. Pullman and D. R. Herschbach, J. Chem. Phys. **90,** 3881 (1989).
[110] V. Aquilanti, D. Ascenzi, D. Cappelletti, and F. Pirani, Nature (London) **371,** 399 (1994).
[111] M. Yamato, S. Okada, V. W.-K.Wu, H. Ohoyama, and T. Kasai, J. Chem. Phys. **113,** 6673 (2000).
[112] H. Ohoyama, M. Yamato, S. Okada, T. Kasai, B. G. Brunetti, and F. Vecchiocattivi, Phys. Chem. Chem. Phys. **3,** 3598 (2001).
[113] W. Allision and E. E. Muschlitz Jr., J. Electron Spectrosc. Relat. Phenom. **23,** 339 (1981).
[114] K. Ohno, S. Matsumoto, K. Imai, and Y. Harada, J. Phys. Chem. **88,** 206 (1984).
[115] H. Yamakado, T. Ogawa, and K. Ohno, J. Phys. Chem. A **101,** 3887 (1997).
[116] T. Pasinszki, H. Yamakado, and K. Ohno, J. Phys. Chem. **97,** 12718 (1993).
[117] K. Kanda, Y. Yamakita, and K. Ohno, Chem. Phys. Lett. **349,** 411 (2001).
[118] S. X. Tian, N. Kishimoto, and K. Ohno, J. Phys. Chem. A **107,** 2137 (2003).
[119] S. X. Tian, N. Kishimoto, and K. Ohno, J. Phys. Chem. A **107,** 485 (2003).
[120] T. Pasinszki, H. Yamakado, and K. Ohno, J. Phys. Chem. **99,** 14678 (1995).
[121] T. Pasinszki, N. Kishimoto, T. Ogawa, and K. Ohno, J. Phys. Chem. A **103,** 7170 (1999).
[122] N. Kishimoto, S. Fukuoka, H. Tanaka, and K. Ohno, J. Electron Spectrosc. Relat. Phenom. **137–140,** 313 (2004).
[123] H. Yamakado, M. Yamauchi, S. Hoshino, and K. Ohno, J. Phys. Chem. **99,** 17093 (1995).
[124] N. Kishimoto, R. Yokoi, H. Yamakado, and K. Ohno, J. Phys. Chem. A **101,** 3284 (1997).
[125] S. X. Tian, N. Kishimoto, and K. Ohno, J. Electron Spectrosc. Relat. Phenom. **127,** 167 (2002).
[126] M. Yamauchi, H. Yamakado, and K. Ohno, J. Phys. Chem. A **101,** 6184 (1997).
[127] N. Kishimoto, T. Oda, and K. Ohno, J. Electron Spectrosc. Relat. Phenom. **137–140,** 319 (2004).
[128] R. Maruyama and K. Ohno, J. Phys. Chem. A **108,** 4211 (2004).
[129] N. Kishimoto, T. Horio, S. Maeda, and K. Ohno, Chem. Phys. Lett. **379,** 332 (2003).
[130] N. Kishimoto, M. Furuhashi, and K. Ohno, J. Electron Spectrosc. Relat. Phenom. **113,** 35 (2000).
[131] N. Kishimoto, Y. Osada, and K. Ohno, J. Phys. Chem. A **104,** 1393 (2000).
[132] N. Kishimoto, Y. Osada, and K. Ohno, J. Electron Spectrosc. Relat. Phenom **114–116,** 183 (2001).
[133] T. Pasinszki, N. Kishimoto, and K. Ohno, J. Phys. Chem. A **103,** 9195 (1999).
[134] K. Ohno, K. Okamura, H. Yamakado, S. Hoshino, T. Takami, and M. Yamauchi, J. Phys. Chem. **99,** 14247 (1995).
[135] A. Borodin, M. Yamazaki, N. Kishimoto, and K. Ohno, J. Phys. Chem. A **109,** 4721 (2005).
[136] H. Yamakado, K. Okamura, K. Ohshimo, N. Kishimoto, and K. Ohno, Chem. Lett. **26**, 269 (1997).
[137] T. Pasinszki, N. Kishimoto, and K. Ohno, J. Phys. Chem. A **103,** 6746 (1999).
[138] K. Imura, N. Kishimoto, and K. Ohno, J. Phys. Chem. A **105,** 6378 (2001).
[139] S. X. Tian, N. Kishimoto, and K. Ohno, J. Phys. Chem. A **106,** 6541 (2002).
[140] S. X. Tian, N. Kishimoto, and K. Ohno, J. Electron Spectrosc. Relat. Phenom. **125,** 205 (2002).
[141] I. Tokue, Y. Sakai, and K. Yamasaki, J. Chem. Phys. **106,** 4491 (1997).
[142] K. Imura, N. Kishimoto, and K. Ohno, J. Phys. Chem. A **105,** 4189 (2001).
[143] K. Ohno, N. Kishimoto, and H. Yamakado, J. Phys. Chem. **99,** 9687 (1995).
[144] N. Kishimoto, K. Ohshimo, and K. Ohno, J. Electron Spectrosc. Related. Phenom. **104,** 145 (1999).
[145] K. Imura, N. Kishimoto, and K. Ohno, J. Phys. Chem. A **105,** 6073 (2001).
[146] K. Imura, N. Kishimoto, and K. Ohno, J. Phys. Chem. A **105,** 10781 (2001).
[147] K. Imura, N. Kishimoto, and K. Ohno, J. Phys. Chem. A **105,** 9111 (2001).
[148] N. Kishimoto, M. Matsumoto, and E. Matsumura, Euro. Phys. J. D **38,** 75 (2006).
[149] S. X. Tian, N. Kishimoto, and K. Ohno, J. Phys. Chem. A **107,** 53 (2003).

[150] Y. Yamakita, M. Yamauchi, and K. Ohno, Chem. Phys. Lett. **322,** 189 (2000).
[151] M. Yamauchi, Y. Yamakita, H. Yamakado, and K. Ohno, J. Electron Spectrosc. Relat. Phenom. **88–91,** 155 (1998).
[152] H. Yamakado, Y. Sawada, H. Shinohara, and K. Ohno, J. Electron Spectrosc. Relat. Phenom. **88–91,** 927 (1998).
[153] N. Kishimoto, Y. Hagihara, K. Ohno, S. Knippenberg, J. P. François, and M. S. Deleuze, J. Phys. Chem. A **109,** 10535 (2005).
[154] A. Borodin, M. Yamazaki, N. Kishimoto, and K. Ohno, J. Phys. Chem. A **110,** 1783 (2006).
[155] H. Tanaka, H. Yamakado, and K. Ohno, J. Electron Spectrosc. Relat. Phenom. **88–91,** 149 (1998).
[156] S. Masuda, M. Aoyama, K. Ohno, and Y. Harada, Phys. Rev. Lett. **65,** 3257 (1990).
[157] M. Yamazaki, N. Kishimoto, and K. Ohno, Euro. Phys. J. D **38,** 47 (2006).
[158] K. Fukui, *Theory of Orientation and Stereoselection* (Springer-Verlag, Berlin, 1975).
[159] R. Hoffmann, Acc. Chem. Res. **4,** 1 (1971).
[160] N. Kishimoto, H. Ogasawara, and K. Ohno, Bull. Chem. Soc. Jpn. **75,** 1503 (2002).
[161] N. Kishimoto, H. Yamakado, and K. Ohno, J. Phys. Chem. **100,** 8204 (1996).
[162] S. X. Tian, N. Kishimoto, and K. Ohno, J. Phys. Chem. A **106,** 7714 (2002).
[163] M. Yamazaki, N. Kishimoto, and K. Ohno, J. Phys. Chem. A **110,** 7097 (2006).
[164] N. Kishimoto and K. Ohno, J. Phys. Chem. A **104,** 6940 (2000).
[165] N. Kishimoto, K. Okamura, and K. Ohno, J. Chem. Phys. **120,** 11062 (2004).
[166] O. Dolgounitcheva, V. G. Zakrzewski, and V. Ortiz, J. Phys. Chem. A **104,** 10032 (2000).
[167] M. S. Deleuze, A. B. Trofimov, and L. S. Cederbaum, J. Chem. Phys. **115**, 5859 (2001).
[168] M. S. Deleuze, J. Chem. Phys. **116**, 7012 (2002).
[169] M. Ehara, Y. Ohtsuka, H. Nakatsuji, M. Takahashi, and Y. Udagawa, J. Chem. Phys. **122,** 234319 (2005).
[170] Y. Hatano, Bull. Chem. Soc. Jpn. **76,** 853, and references cited therein (2003).
[171] W. Kischlat and H. Morgner, Z. Phys. A **312,** 305 (1983).
[172] A. Benz, O. Leisin, H. Morgner, H. Seiberle, and J. Stegmaier, Z. Phys. A **320,** 11 (1985).
[173] A. Benz and H. Morgner, Mol. Phys. **58,** 223 (1986).
[174] S. X. Tian, N. Kishimoto, and K. Ohno, Chem. Phys. Lett. **365,** 40 (2002).
[175] K. Imura, N. Kishimoto, and K. Ohno, J. Phys. Chem. A **106,** 3759 (2002).
[176] N. Kishimoto, E. Matsumura, K. Ohno, and M. S. Deleuze, J. Chem. Phys. **121,** 3074 (2004).
[177] H. Tanaka, R. Maruyama, Y. Yamakita, H. Yamakado, F. Misaizu, and K. Ohno, J. Chem. Phys. **112,** 7062 (2000).
[178] R. Maruyama, H. Tanaka, Y. Yamakita, F. Misaizu, and K. Ohno, Chem. Phys. Lett. **327,** 104 (2000).
[179] K. Fukui, Int. J. Quantum. Chem. **12,** 277 (1977).
[180] K. Fukui, T. Yonezawa, and H. Singu, J. Chem. Phys. **20,** 722 (1952).
[181] R. B. Woodward and R. Hoffman, Angew. Chem. Int. Ed. Engl. **8,** 781 (1969).
[182] M. Yamazaki, T. Horio, N. Kishimoto, and K. Ohno, submitted for publication.
[183] T. Ebding and A. Niehaus, Z. Physik. **270,** 43 (1974).
[184] K. Mitsuke, K. Kusafuka, and K. Ohno, J. Phys. Chem. **93,** 3062 (1989).
[185] F. Tuffin, A. Le Nadan, and J. Peresse, J. Phys. (Les Ulis, Fr.) **46,** 181 (1985).
[186] K. Ohno, Theor. Chim. Acta **74,** 239 (1988).
[187] T. Ishida and K. Ohno, Int. J. Quantum Chem. **35,** 257 (1989).
[188] W. Kohn and L. J. Sham, Phys. Rev. **140,** A1133 (1965).
[189] R. G. Parr and W. Yang, *Density-functional Theory of Atoms and Molecules* (Oxford University Press, New York, 1989).
[190] A. D. Becke, J. Chem. Phys. **98,** 5648 (1993).
[191] D. Feller, C. M. Boyle, and E. R. Davidson, J. Chem. Phys. **86,** 3424 (1987).
[192] H. Nakatsuji, Chem. Phys. Lett. **59,** 362 (1978).
[193] H. Nakatsuji and K. Hirao, J. Chem. Phys. **68,** 2053 (1978).
[194] H. Morgner, Adv. At. Mol. Opt. Phys. **42B,** 387, and references cited therein (2000).
[195] Y. Harada, S. Masuda, and H. Ozaki, Chem. Rev. **97,** 1897, and references cited therein (1997).